ACTIVE CONTROL OF ENVIRONMENTAL NOISE, VI: PERFORMANCE OF A FUNDAMENTAL FREE–FIELD SOUND CANCELLING SYSTEM

S. E. WRIGHT AND H. ATMOKO

*School of Engineering, University of Huddersfield, Huddersfield HD1 3DH, England.
E-mail: selwyn.wright@ntlworld.com*

Before the adaptive cancellation performance of multichannel free-field acoustic systems could be evaluated in detail, it was considered prudent to establish first the performance of a single channel free-field cancelling system. The adaptive theory for this basic system, including the stability process, is described. Measured adaptive performance is given confirming the theory.

The concept of stability bands and their prediction is considered. The bands are a consequence of phase differences between the primary source and secondary cancelling field, generated by the transfer functions of the control system. At the edge of these stability bands satellite pole frequencies "beat" with the cancelling frequency, generated by the zeros, to produce side bands. The relation between the stability bandwidth and the adaptive speed, in terms of reference signal strength and adaptive step size, are investigated.

The sound generation and cancellation performance of this basic canceller are then considered. The acoustic sound field directivity characteristics are similar to that of a dipole, tripole or quadrupole type source, depending on the primary–secondary source separation distance. The acoustic shadow characteristics are established in detail and compared with measurement. Good agreement is obtained.

© 2001 Academic Press

1. INTRODUCTION

This is paper VI in a series covering the development of electronically controlled acoustic shadows for environmental noise reduction. The basic wave theory using computer modelling, and point acoustic sources in free-field was reported in reference [1]. The theory was extended to complex high-frequency sound from large non-compact sources in reference [2]. The implementation of the wave theory into hardware was considered in reference [3]. The effect of three-dimensional primary sources, out-of-phase primary sources, reflecting surfaces and steady wind on the shadow generation has been considered in reference [4]. The effect of environmental change on the stability of adaptive process was considered in reference [5].

The control algorithms for active noise control systems, in enclosures, have been extensively investigated (see for example Elliott *et al.* [6] and Kuo and Morgan [7]). Free-field systems use similar kinds of algorithms, although the free-field plant (propagation space) is quite different than that in enclosures. In enclosures the sound fields are usually complex, having standing waves and diffuse sound, with secondary sources and detectors non-aligned. This situation results in cancellation regions limited to a fraction of an acoustic wavelength as considered by Nelson and Elliott [8] and Abbot [9].
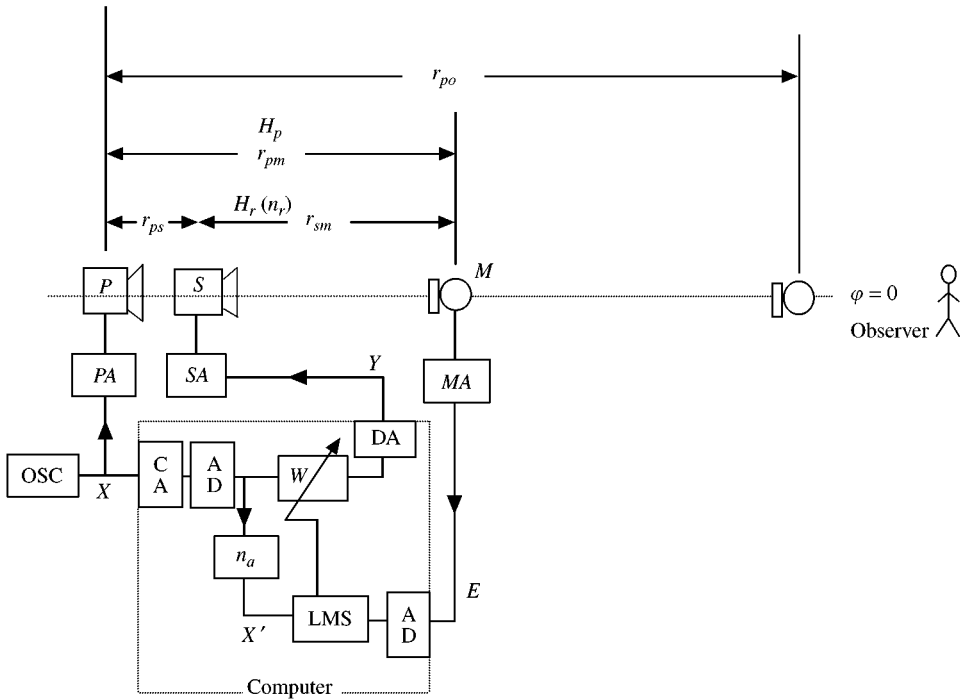
Figure 1. Basic free-field cancelling system.

In this present investigation, the basic theory for a single channel free-field cancelling system is established. The system, as illustrated in Figure 1, comprises a cancelling secondary source (loudspeaker) placed close to the primary (unwanted) source to be cancelled (represented here by another loudspeaker) and a detection system (microphone) aligned with the two sources, placed some distance away, in the direction of required cancellation (successive axial alignment with the primary source). This ensures cancellation in the direction of wave propagation, which then generates an acoustic shadow along the wave direction extending to large distances from the primary source i.e., not restricted to a fraction of an acoustic wavelength.

The plant to be analyzed, is also modelled in Figure 1. It consists of the transfer functions of the electromechanical system (cancelling loudspeaker H_c, detection microphone H_m, amplifiers and antialiasing/quantization filters in the computer H_f). The transfer function of the propagation environment H_r between the secondary loudspeaker and the detection microphone basically represents a phase retardation or delay. The propagation transfer function H_p between the primary source and the microphone is also basically a delay. P is the primary noise source to be cancelled. The source can be generated by a signal generator (oscillator) which drives both the loudspeaker (for the primary field) and the input to the computer, or it can be a real acoustic noise source, in which case a synthesized reference signal synchronized to the primary source is required (not shown). W is the adaptive element in the system. It is a monochromatic two-tap (coefficient) FIR filter, whose phase difference between its two inputs is limited to $90°$. The filter, therefore, can only adapt to within $\pi/2$ rad of the reference signal.

Thus, there is a requirement for some other method to offset the large phase delays generated by the system transfer functions. H_a is introduced as a secondary path simulation

simplification, used in the filtered X algorithm. This is required to maintain stability in the time domain, first used by Widrow *et al.* [10] and Burgess [11]. For a single cancelling frequency, H_a can be a simple delay, as considered by Ziegler [12]; this is, in this case, equivalent to the propagation delay H_r. However, for a single frequency, it is not essential to match this delay exactly, providing the delay is within one acoustic wavelength (2π rad). Therefore, H_a is used here simply as a phase adjustment to tune in a particular stability region. X is the primary source reference signal and X' is the filtered reference signal after it has been modified by H_a.

In the paper, section 2 considers the adaptive theory for this system and section 3 considers the measured adaptive performance. Section 4 is concerned with the acoustic theory of the radiation process for the basic canceller and section 5 deals with the measured acoustic performance.

2. ADAPTIVE THEORY

In this section the theory of the basic canceller is considered. It establishes the transfer functions of the adaptive system, both open and closed loop, the resulting stability bands, satellite pole frequencies, the effect of sample delay and the prediction of the stability bands of a real system.

2.1. SYSTEM TRANSFER FUNCTION

The equivalent open-loop transfer function between the primary source signal $d(n)$ and the cancelling signal $y(n)$, for a single-frequency, single-channel canceller was first derived by 'Bernie' Widrow, the father of adaptive control [13], as

$$G(z) = \frac{D(z)}{Y(z)} = \mu A^2 \frac{(z\cos\theta - 1)}{(z^2 - 2z\cos\theta + 1)}. \tag{1}$$

The situation is illustrated in Figure 1, where H_p, H_f, H_c, H_r and H_a are all unity making zero phase around the plant. The upper case symbols imply Z transformed variables, μ is the adaptive step size, and A is the amplitude of the reference signal input to the computer (X). Individual values of μ and A are not important; it is the cancelling strength μA^2 that counts, represented by β. Also, $\theta = \omega_{ac}T_n$, where $\omega_{ac} = 2\pi f_{ac}$ is the cancelling frequency and T_n is the sampling period, giving the acoustic cancelling frequency angle as

$$\theta = \omega_{ac}T_n = 2\pi f_{ac}/f_n. \tag{2}$$

The closed-loop transfer function given by the error signal $e(n)$, formed from the difference between the primary signal to be cancelled $d(n)$ and the cancelling signal $y(n)$, divided by $d(n)$ then follows from equation (1), as

$$H(z) = \frac{E(z)}{D(z)} = \frac{1}{1 + G(z)} = \frac{(z^2 - 2z\cos\theta + 1)}{(z^2 - 2z\cos\theta + 1 + \beta(z\cos\theta - 1))}. \tag{3}$$

The conjugate zeros in the numerator, which lie on the unit circle in the z-plane symmetrical about the real axis, determine the cancelling frequency. The conjugate poles in the denominator modify the frequency response. For small β, the conjugate pole pair lie close to the conjugate zeros on the zero-origin radius. They make the same frequency angle θ

with the real axis as the cancelling frequency angle. As the cancelling strength β increases, the conjugate poles move inwards away from the unit circle along the radius, through the origin at $\beta = 1$, and then pass along the negative real axis out through the unit circle at $\beta = 2$, as given by Kuo and Morgan [7]. Thus, this system can only become unstable when $\beta \geqslant 2$. The further the pole lies from the zero (large β), the faster the adaptive response and the wider the notch bandwidth.

2.2. STABILITY BANDS

Equation (3) is for an in-phase canceller, having no physical plant, which is not a realistic situation in this application. For a practical system, the transfer functions H_p, H_f, H_c and H_r, in Figure 1, are now no longer equal to unity. Fortunately, the cancellation process will still continue for a net phase difference ϕ generated by these transfer functions, relative to the primary field. In this situation, a series of alternate stable and unstable bands are now generated as ϕ changes by multiples of π. To investigate the properties of these stability bands, a result derived by Elliot and Nelson [14], for the assessment of errors between the estimated and the actual secondary path of control plant, is used. Equations (1) and (3) now become

$$G(z) = \frac{D(z)}{Y(z)} = \beta \, \frac{(z \cos(\theta - \phi) - \cos\phi)}{(z^2 - 2z \cos\theta + 1)},$$

$$H(z) = \frac{E(z)}{D(z)} = \frac{1}{1 + G(z)} = \frac{(z^2 - 2z \cos\theta + 1)}{(z^2 - 2z \cos\theta + 1 + \beta[z \cos(\theta - \phi) - \cos\phi])}. \tag{4}$$

This system can now become unstable, even for small β, if $\phi > |\pi/2|$, as the conjugate poles can now pass directly out of the unit circle without moving via the origin.

Initially, the adaptive filter W produces the anti-phase in $Y(z)$ to cancel the primary field $D(z)$. For zero phase difference $\phi = 0$ or 2π, the cancelling system is then operating in the middle of its stability region with the same frequency as the cancelling frequency (same angle θ). As the phase angle ϕ increases, the poles now move around phase contour rings situated around the upper zero, in a clockwise direction, and anticlockwise around the lower zero, both zeros situated on the unit circle. The situation is computed in Figure 2. In Figure 2(a), the z-plane is given for a complete phase circle $\phi = 0 \to 2\pi$ (6·28) rad for cancelling strengths $\beta = 0·2$, 0·4, 0·8 and a cancelling frequency of 400 Hz. The system becomes unstable when the poles move outside the unit circle.

It can be seen that there is a consecutive series N, of alternative stable and unstable bands of width π, as the phase lag ϕ progressively increases. For small β, the satellite pole phase rings are small and concentric around the zeros. As β increases, the size of the phase contour rings increases and distorts towards the origin. The conjugate poles closest to the real axis become real and join the upper and lower phase circles together. Thus, one large enclosed region around the conjugate zeros is formed as computed for $\beta = 0·8$ in the figure.

Eventually, the stability bands become severely asymmetrical about $\phi = 0$. For example, the lower frequency pole position on the right-hand negative phase side of the upper pole phase circle, corresponding to $\phi = -\pi/2$ or $3/4(2\pi) = 4·71$ rad, passes around the unit circle, in a clockwise direction, as β increases, before exiting along the positive real axis at $\beta = 0·65$, (not shown). For $\phi = 0$ or 2π rad (zero phase situation), the pole passes through the origin at $\beta = 1$ and then travels along the negative real axis before exiting the unit circle at $\beta = 2$, shortening the negative side of the stability band. For $\phi = +\pi/2$ radians, the
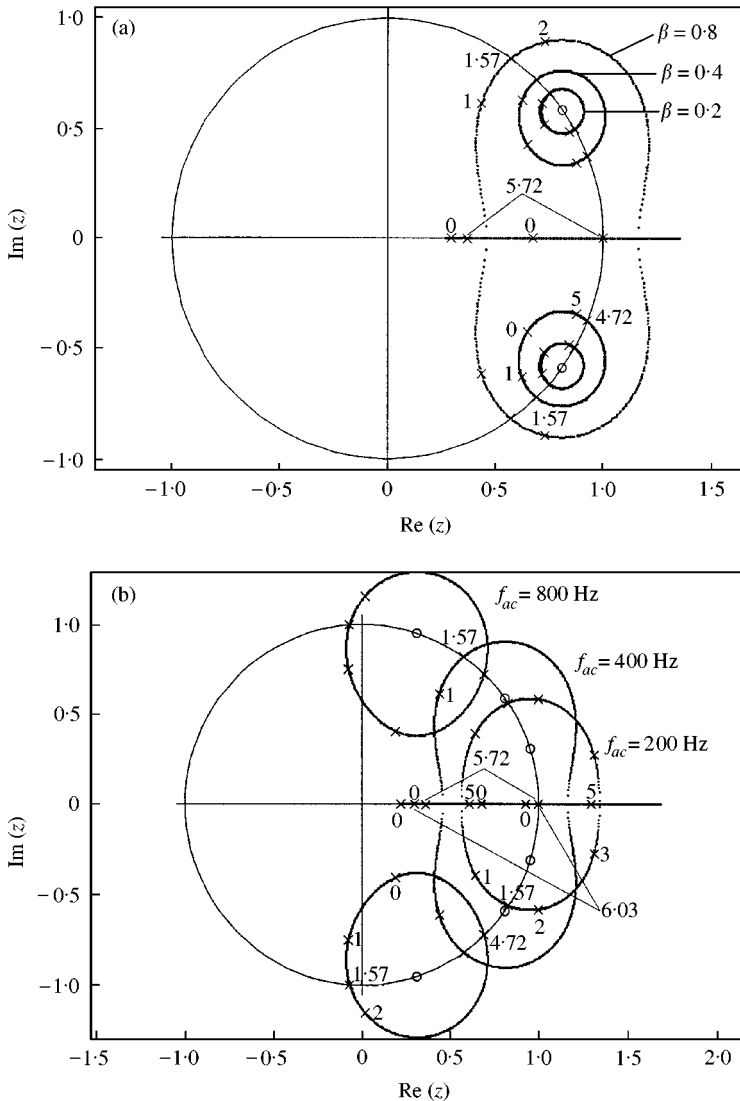
Figure 2. Pole zero location in the z-plane showing the satellite pole phase contour rings surrounding the cancelling zeros $\phi = 0 \rightarrow 6\cdot28$ (2π). (a) The phase rings for values of cancelling strength $\beta = 0\cdot2$, $0\cdot4$ and $0\cdot8$ for a cancelling frequency of $f_{ac} = 400$ Hz. (b) The phase rings for three cancelling frequencies $f_{ac} = 200$, 400 and 800 Hz for $\beta = 0\cdot8$, $f_n = 4000$ Hz. $\bigcirc$, zero location; $\times$, pole location.

higher frequency pole position on the left-hand side of the upper phase circle rotates anticlockwise around the unit circle, exiting along the negative real axis at $\beta = 6\cdot147$, as shown later in Figure 3, extending the positive side of the stability band.

Thus, the stability band starts to shrink at $\phi = -\pi/2$ ($1\cdot57$) rad at $\beta = 0\cdot65$ and ends up at zero bandwidth at $\phi = +\pi/2$ rad and $\beta = 6\cdot147$. The stability bandwidths (corresponding to the satellite pole positions lying within the unit circle) are found from subtracting the difference in ϕ between poles entering and leaving the unit circle from 2π rad. They are $\Delta\phi = 6\cdot28 - (4\cdot72 - 1\cdot57) \approx 3\cdot14$, $6\cdot28 - (4\cdot72 - 1\cdot57) \approx 3\cdot14$ (same as previous value) and $6\cdot28 - (5\cdot72 - 1\cdot57) = 2\cdot13$ rad, respectively, for $\beta = 0\cdot2$, $0\cdot4$ and $0\cdot8$; i.e., the contraction does not start until $\beta > 0\cdot4$.

Figure 2(b) shows the situation for three cancelling frequencies 200, 400 and 800 Hz at a cancelling strength of $\beta = 0\cdot8$. It can be seen that the stability bandwidths increase considerably with increasing frequency; they are $\Delta\phi = 6\cdot28 - (6\cdot03 - 1\cdot57) = 1\cdot82$, $6\cdot28 - (5\cdot72 - 1\cdot57) = 2\cdot13$ and $6\cdot28 - (4\cdot72 - 1\cdot57) = 3\cdot13$ rad. The band expansion continues up to $f_n/4$ (1000 Hz), where it starts to reduce towards $f_n/2$, the Nyquist frequency (not shown). The corresponding onset of zero bandwidths occur at rather large values of β; they are $\beta_{zbw} = 12$, $6\cdot147$ and $2\cdot7$, for the three frequencies respectively (not shown).

2.3. SATELLITE FREQUENCIES

For non-zero phase angle ϕ, the satellite pole frequency angle is now no longer equal to the cancelling frequency angle θ and therefore, is associated with a different frequency. For small values of β, the satellite poles, lying on the phase circles around the zeros on the unit circle, make an angle $\Delta\theta$ with the cancelling angle θ, producing with a little geometry, a modulation frequency of

$$\omega_{mod} = f_n \Delta\theta = f_n \tan^{-1}\left[\frac{R\sin\phi}{1 - R\cos\phi}\right]$$

$$\approx f_n R \sin\phi \quad \text{for } R \text{ small}, \tag{5a}$$

where R, which is a function of β, is the radius of the phase circle. The individual satellite pole frequency corresponding to each edge of the stability band, $\phi = \pm\pi/2$, is then

$$\omega_{sat} = \omega_{ac} + \omega_{mod} = (\theta_{ac} + \Delta\theta)f_n$$

$$\approx [\theta_{ac} + R\sin\phi_\pm)]f_n$$

$$\approx [\theta_{ac} \pm R_\pm]f_n, \tag{5b}$$

where $R_\pm$ is the radius each side of the stability band. Finally, sum and difference frequencies of the cancelling frequency (side bands) which occur simultaneously, arise at each edge of the stability band given by

$$\omega_{sb} = \omega_{ac} \pm \omega_{mod}. \tag{5c}$$

Small values of β (small R) and small ϕ yield small sum and difference frequencies close to the cancelling frequency which decay rapidly, making the frequencies difficult to observe. Increasing β gives increased phase circle radius and increased circle distortion, resulting in marginally higher and lower damped satellite frequencies at each side of the cancelling frequency. At the edge of the stability band, the side band frequencies remain undamped, leading to additional unwanted frequencies in addition to the frequency to be cancelled.

Figure 3(a) shows the situation in the frequency domain for a cancelling frequency of $f_{ac} = 400$ Hz, $\omega_{ac} = 2\pi f_{ac} = 2\cdot5$ krad. If the sampling frequency $f_n = 4$ kHz, then the angle of the cancelling zero is $\theta_{ac} = \omega_{ac}T_n = 0\cdot628$ rad or, from equation (3), $360(f_{ac}/f_n) = 36°$. The pole satellite frequencies f_{sat} on the upper side of the cancelling frequency, at $\phi = +\pi/2$, for various values of β, are given. The maximum frequency corresponding to $\theta_{sat} = \pi$ is, from equation (2), $f_{sat} = f_n/2 = 2$ kHz, the Nyquist value. Figure 3(b) shows the corresponding pole positions in the z-plane as β is varied. These figures confirm the surprising result that at the upper frequency edge of the stability band ($\phi = +\pi/2$), the system can remain stable for
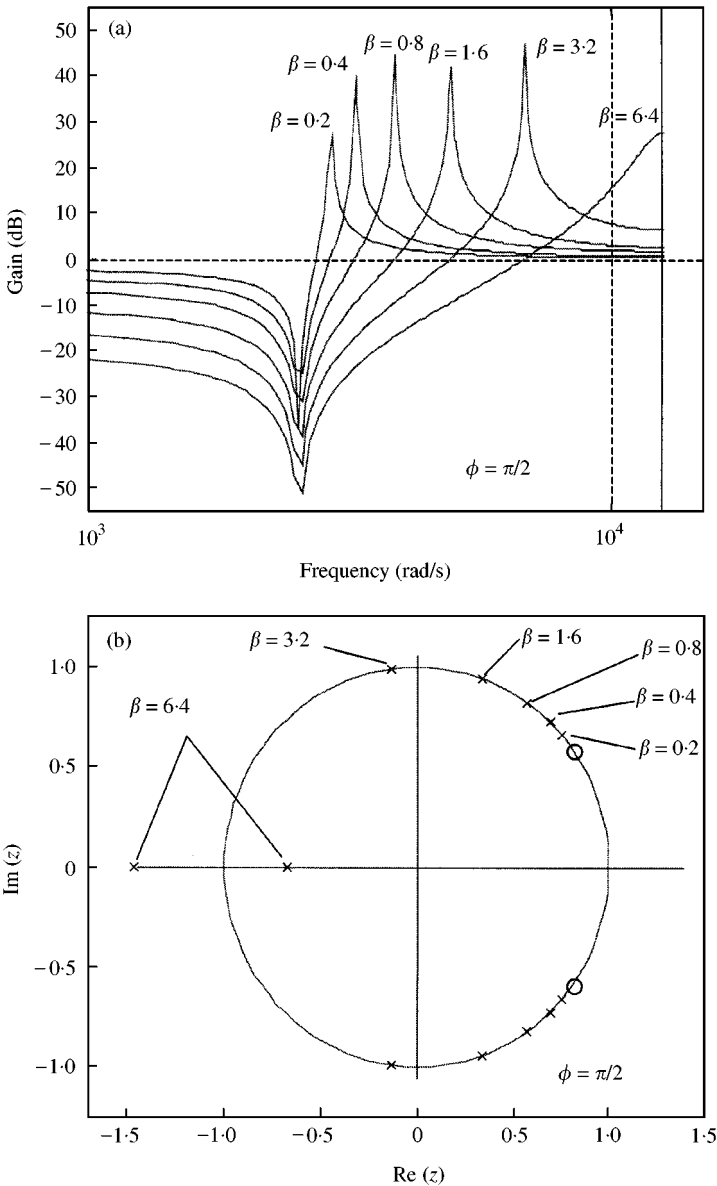
Figure 3. Satellite pole frequencies. (a) Frequency domain for satellite frequencies (upper frequency side of zero, $\phi = \pi/2$) as a function of β from 0·2 to 6·4, $f_{ac} = 400$ Hz, $f_n = 4000$ Hz. (b) The corresponding pole positions in the z-domain.

β values greater than 6, whereas the classical value, in the centre of the band ($\phi = 0$), remains stable only for values of β up to 2.

2.4. SAMPLE DELAY

The analysis first considered the rather unrealistic zero phase adaptive system without a physical plant. The more practical case of phase differences, generated by the transfer functions in real plants, was then considered in the previous section. Finally, the dominant

effect of propagation delay in these systems is now considered. Step increases in phase can be introduced through n samples delay in the closed-loop system. In this case, equation (4) becomes

$$H(z) = \frac{1}{(1 + z^{-n}G(z))} = \frac{(z^2 - 2z\cos\theta + 1)z^n}{\{(z^2 - 2z\cos\theta + 1)z^n + \beta[z\cos(\theta - \phi) - \cos\phi]\}}. \tag{6}$$

For evaluation purposes, z^n is used rather than z^{-n} making n positive for a delay. This equation contains additional zeros situated at the origin and additional poles. The additional conjugate poles move into the ϕ phase contour rings. The remaining poles move in the vicinity of the zeros at the origin. The situation obviously becomes more complex as the order n increases. Figure 4(a) shows the computed phase contour rings ϕ for one sample
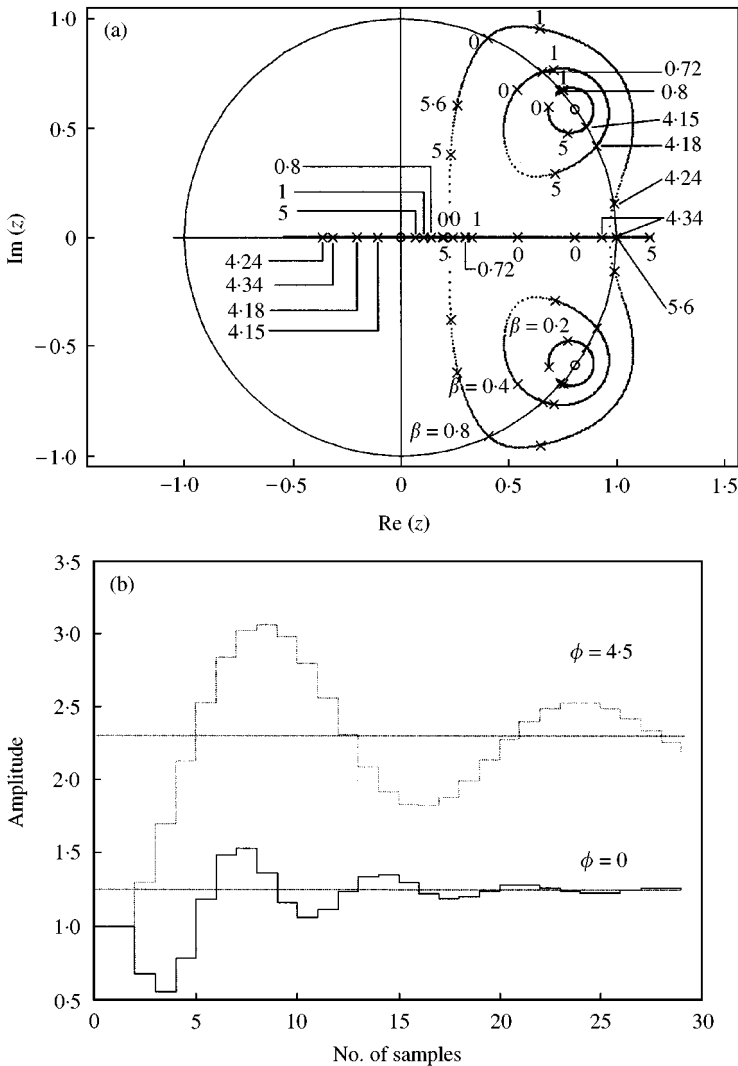

Figure 4. Computation for one sample delay $n = 1$. (a) Pole zero location in the z-plane for $n = 1$, $\phi = 0 \to 6\cdot28$ (2π), $\beta = 0\cdot2$, $0\cdot4$ and $0\cdot8$, $f_{ac} = 400$ Hz, $f_n = 4000$ Hz. (b) The corresponding time histories to a step response for pole positions on each side of the stability band near to the inner edge of the unit circle. $\beta = 0\cdot4$ and $\phi = 0$ and $4\cdot5$.

delay, $n = 1$ and a cancelling frequency of 400 Hz. The poles are rotated by approximately $\phi = 0.63$ rad, given by the equivalence $\phi \equiv \omega t$, where $t = nT_n$ and from equation (2)

$$\phi \equiv n(2\pi f_{ac}/f_n) = n\theta, \; \theta = 0.63. \tag{7}$$

Here, the stability bandwidth also shrinks as β increases. For $\beta = 0.2$ the stability bandwidth is $\Delta\phi = 6.28 - (4.15 - 0.8) = 2.93$ rad. For $\beta = 0.4$, the stability bandwidth is $\Delta\phi = 6.28 - (4.18 - 0.72) = 2.82$ rad. However, for $\beta = 0.8$ complex band splitting occurs i.e., the band is unstable for $\Delta\phi = 0 \rightarrow 4.24$ and $4.34 \rightarrow 5.6$ (1.26) with a stable region $4.24 \rightarrow 4.34$ (0.1) in between, making the stable bandwidth $\Delta\phi = 6.28 - (4.24 + 1.26) = 0.78$ or $6.28 - 5.6 + 0.1 = 0.78$ rad. The onset of zero bandwidth (not shown) for the three cancelling frequencies $f_{ac} = 200$, 400 and 800 Hz, corresponds to $\beta_{zbw} = 0.95$, 1, 1.6 respectively. These are considerably lower than for zero sample number $n = 0$ computed in Figure 2(a) for the same frequencies ($\beta_{zbw} = 12$, 6.147 and 2.7 respectively).

Figure 4(b) shows the computed time domain response to a unit step input. For $\beta = 0.4$ and $\phi = 4.5$ and 0, the satellite pole positions for the lower and upper stability band frequencies are just inside the unit circle for both the cases. The responses are therefore just stable, with decaying lower and upper satellite pole frequency responses at each edge of the stability band given by $f_{sat} = 1/n\,T_n = f_n/n = 4000/16 = 250$ and $4000/7 = 570$ Hz. n is the sample number and T_n is the sample period (spacing of sampling steps in the figure). This would give lower and upper modulation frequencies of $f_{mod} = 400 - 250 = 150$ and $570 - 400 = 170$ Hz, if excited with a 400 Hz cancelling frequency, rather than a step function. The equivalent phase circle radius, at the edge of each stability band, from equation (5a), is $R = \omega_{mod}/f_n \equiv 360°(f_{mod}/f_n) = 13.5$ and $15.3°$, respectively, the angles of which can be checked from Figure 4(a). Other computations for higher order delays show similar characteristics with $\phi \approx n\theta$ phase circle rotations, band splitting and zero band width occurring close to $\beta = 1$, rather than the very large values in the zero sample delay case.

Figure 5(a) shows the phase contour rings for sample delays, $n = 2$, 4 and 8, for a cancelling strength $\beta = 0.4$. The poles now leave the real axis, for large n, to form "daisy chain" phase rings close to the inside of the unit circle for large β and high frequencies. However, at no time do the poles leave the unit circle, except to pass around the cancelling zero. The decreasing stability bandwidths for $\beta = 0.4$ and the three consecutively increasing delays are $\Delta\phi = 5.95 - 3.8 = 2.15$, $\Delta\phi = 4.7 - 3.2 = 1.5$ and $\Delta\phi = 1.4 - 1.4 = 0$. Figure 5(b) shows the phase contours for three cancelling frequencies $f_{ac} = 200$, 400 and 800 Hz for $n = 4$ and $\beta = 0.4$. The decreasing stability bandwidths for the consecutively increasing frequencies are $\Delta\phi = 5.5 - 3.8 = 1.7$, $\Delta\phi = 4.7 - 3.1 = 1.6$ and $\Delta\phi = 2.05 - 0.55 = 1.5$ rad. The β values for the onset of zero bandwidth for the three cancelling frequencies (not shown) are respectively $\beta_{zbw} = 0.55$, 0.6, and 0.7. Thus it can be seen that at low n, the β values for zero bandwidth are large and vary considerably. As n increases, the β values become more similar and reduce below $\beta = 1$ with increasing order.

2.5. STABILITY BAND PREDICTION

The theory for predicting the actual stability bands for the schematic system shown in Figure 1 is given in reference [3], in particular by equation (34) as

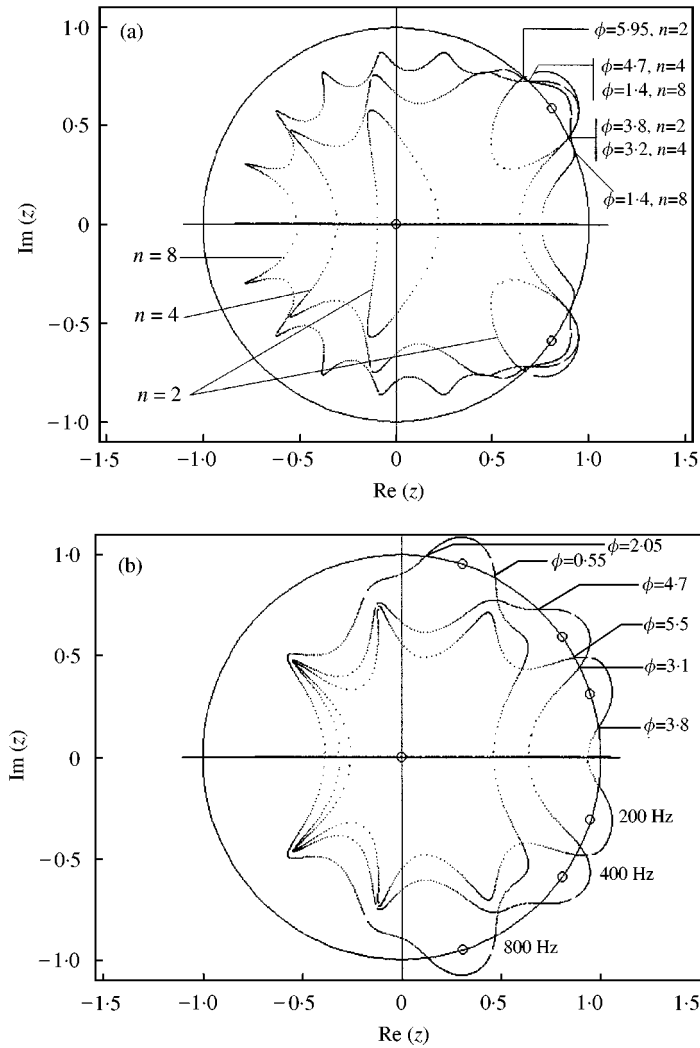$$n_a = \left(\frac{N - N_{em}}{f_{ac}} + \frac{r_{sm}}{c_0} \right) f_n \tag{8}$$

Figure 5. Satellite pole phase contour rings for large n. (a) The contours for three sample delay numbers $n = 2$, 4 and 8 for $\beta = 0.4$. (b) The contours for three cancelling frequencies $f_{ac} = 200$, 400 and 800 Hz for $n = 4$ and $\beta = 0.4$.

or

$$n_a = (N - N_{em})f_n/f_{ac} + n_r \quad \text{where } n_r = (r_{sm}/c_0)f_n. \tag{9}$$

These equations predict the contours of the centre of the stable regions (N integer). They depend on the electromechanical phase transfer function N_{em}, measured in integers of 2π rad, the propagation distance r_{sm} between the secondary speaker and the detection microphone, the acoustic source cancellation frequency f_{ac}, the speed of sound c_0, and the sampling frequency f_n. n_r is the number of retarded samples through the propagation delay between the speaker and microphone, and n_a is the number of advance samples used in the LMS algorithm. For $n_a = n_r$, the sample advance compensates for the propagation delay. For no propagation delay and no sample advance $n_a = n_r = 0$, $N = N_{em}$ and the contours are determined solely by the electromechanical phase transfer function of the system N_{em}.

Equations (8) and (9) predict the specific stability bands of a practical system. As the cancelling frequency f_{ac} increases, the frequency angle θ in equation (2) increases and the unit circle zeros move around the unit circle, the upper zero in an anticlockwise direction and the lower zero in a clockwise direction. Simultaneously, the system phase ϕ increases, through the delay in the system transfer functions, rotating the upper satellite pole around the zero in a clockwise direction and the lower satellite pole in an anticlockwise direction, analogous to moons rotating around planets rotating around the sun. Successive rotations N around the pole phase contour rings, is equivalent to moving across N 2π stability regions for a fixed sample number n_a, in equation (8) and measured (horizontally) in Figure 6(a), to be discussed later. Changing the n_a number for a fixed frequency is equivalent to a discrete rotation of $n\theta$ according to equation (7) and measured (vertically) in Figure 6(a). For increasing values of β the phase contours become non-circular and the stability bands shrink towards zero.

3. MEASURED ADAPTIVE PERFORMANCE

After establishing the adaptive theory, the measured adaptive performance is now considered. The stability bandwidth, cancellation convergence, cancellation frequency distorsion and the adaptive speed are investigated.

3.1. MEASUREMENT DETAILS

Figure 1 illustrates the system set-up. The amplitude A of the reference oscillator signal (X) supplied to the computer, is measured in mV. The programmable gain (steps of 1, 10 and 100) of the computer input amplifier CA was set at 10, and an upper cut-off frequency of the computer antialiasing/quantization filters adjusted to 800 Hz. The output from the A–D converters is 10 V p–p, making a maximum signal input to the computer of 1V p–p without signal clipping. The reference signal also drives the primary source through a power amplifier whose gain PA can be varied arbitrarily between 0 and 8. This alters the output from the primary source, increasing the sound level to be cancelled without changing the reference signal to the computer. Also, the secondary sources have an in-built amplifier SA whose setting can be varied between 0 and 8. Decreasing SA decreases the cancelling field for the same reference amplitude A (same primary field). This in turn increases the filter coefficients, automatically, to restore the secondary field back to its previous value. SA is kept low (4) to operate the coefficients close to their maximum dynamic range. This gives a good system signal/noise ratio. The microphone amplifier gain MA is fixed at 100.

3.2. STABILITY BANDWIDTH

Figure 6(a) shows the actual measured stability band positions and bandwidths by measuring the frequency range over which the system remains stable, as discussed in the theory in section 2.2. Here, the bands are measured for three n_a numbers 10, 20 and 30, over a frequency range 0–1100 Hz. The stability band numbers over this range are $N = -3$ to 2, whose centre positions are predicted by equation (8). These bands are measured for a secondary source–microphone propagation distance of $r_{sm} = 1$ m, adaptive step size $\mu = 0.1$ and primary source power amplifier position $PA = 2$. The reference signal amplitude at the input to the computer is $A = 20$ mV, defining the measured cancellation strength β for this particular experimental set-up as $\beta = \mu A^2 = 0.04 \times 10^{-3}$.
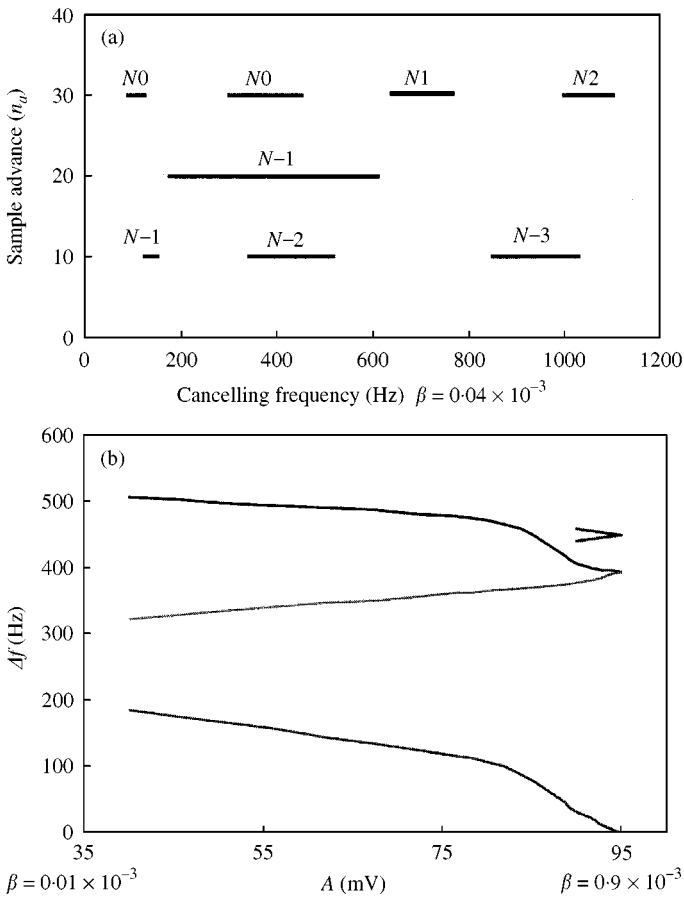
Figure 6. Typical stability bands and their contraction. (a) Stability band map (sample advance n_a versus cancelling frequency in Hz for multiples of $N\,2\pi$ phase) $A = 20$ mV, $\mu = 0.1$, $(\beta = 40 \times 10^{-6})$, $r_{sm} = 1$ m. (b) Typical stability band contraction Δf (Hz) with increase in reference input A (mV). Top of the figure gives actual edges of the stability band, showing band splitting near zero bandwidth, $N - 2$, n_a 10.

At this low cancellation strength, the stability regions have a near full bandwidth of $\phi = \pi/2$. As β increases, the stability bands progressively shrink and finally disappear (have zero bandwidth) according to the properties as discussed in section 2.2. The $N - 0$ and $N - 1$ bands, at approximately 100 Hz, shrink to zero first: at about $A = 10$ and 40 mV respectively. The mid-frequency bands disappear between 80 and 130 mV, and $N2$ and $N - 3$ bands, at around 1000 Hz, are the last to go at about 170 and 150 mV respectively. This gives an operational range of β from 0.01×10^{-3} to 3×10^{-3}. Note the band persistence, with increasing frequency, for a given reference A, as predicted in Figures 2(b) and 5(b). The sequence of stability band numbers in Figure 6(a) may appear irrational; however, the logic is more apparent in the bigger picture revealed for example in reference [5]. Although the stability bands are unique, i.e., they have different eigenvalues, fortunately they tend in general to have similar properties.

Figure 6(b) shows the typical upper and lower frequency band extent (for example, the $N - 2$, n_a10 stability band) as a function of reference signal amplitude A in mV. Again, $\mu = 0.1$ and $r_{sm} = 1$ m. At low A, the centre band cancelling frequency f_{ac} is 430 Hz and has a full bandwidth of $\phi = \pi$. As A increases, it can be seen that the band contracts
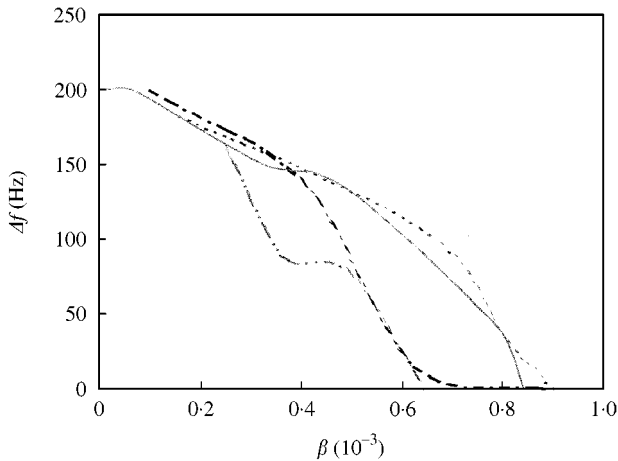
Figure 7. Stability band width Δf versus β showing the data collapse on the parameter $\beta = \mu A^2$ as μ is varied by 10^3, $N-2$, n_a 10, $\mu = 0.01$, 0.1, 1, 10, $r_{sm} = 1$ m.

asymmetrically compared to the convergence zero bandwidth centre frequency $f_{ac} = 395$ Hz. The upper side reduces in frequency over a larger range than the lower side increases, as explained in section 2.2. Band splitting is also evident at high A, just before the band shrinks to zero, as explained in section 2.4. The lower curve shows the actual bandwidth Δf plotted in Hz against the reference amplitude A in mV.

Figure 7 shows the measured stability bandwidths for the same $N-2$, $n_a 10$ band as a function of β for four values of $\mu = 10$, 1, 0.1, 0.01. The actual variations in individual trajectories are not important. What is important is that the data collapses, for a large variation (1000-fold) in μ, on the parameter $\beta = \mu A^2$ (adjusting A accordingly). The zero bandwidth convergence point corresponding to $\beta \approx 1$ in the theory section (Figure 4), corresponds to about $\beta_{zbw} \approx 0.8 \times 10^{-3}$ in the measurements, for this particular frequency band and equipment settings. For large μ, small values of A, mV's have to be used. For $\mu = 0.001$, values up to $A = 1$ V were used. Computationally, there is nothing sacrosanct regarding the values of μ and the equivalent A being less than unity. Here, it is the product μA^2 that is important.

3.3. ADAPTIVE CONVERGENCE

Figure 8 shows the typical cancellation convergence at the centre of the $N-2$, $n_a 10$ stability band, ($f = 430$ Hz) for three low values of the reference signal amplitude $A = 10$, 20 and 40 mV, where $PA = 5$, $r_{sm} = 1$ m, $\mu = 0.1$, and the sampling frequency $f_n = 4$ kHz. The corresponding $\beta = \mu A^2$ values are 0.01×10^{-3}, 0.04×10^{-3} and 0.16×10^{-3} respectively, well below $\beta_{zbw} \approx 0.8 \times 10^{-3}$. At the centre of the band, the error signal E (difference between the primary and secondary sound at the microphone, shown in Figure 1) decays exponentially, its decay rate increasing with reference amplitude A, where j and k are sample numbers. The adaptive speed (error decay rates) is considered in detail in section 3.5. The main point regarding this figure is that operating in the centre of the stability band produces no frequency modulation and no side band generation. Also shown in Figure 8 is the value of the taps (coefficients) of the two-tap FIR filter W. For an optimum system (90° phase between tap inputs and the system operating in the middle of the stability band), the tap
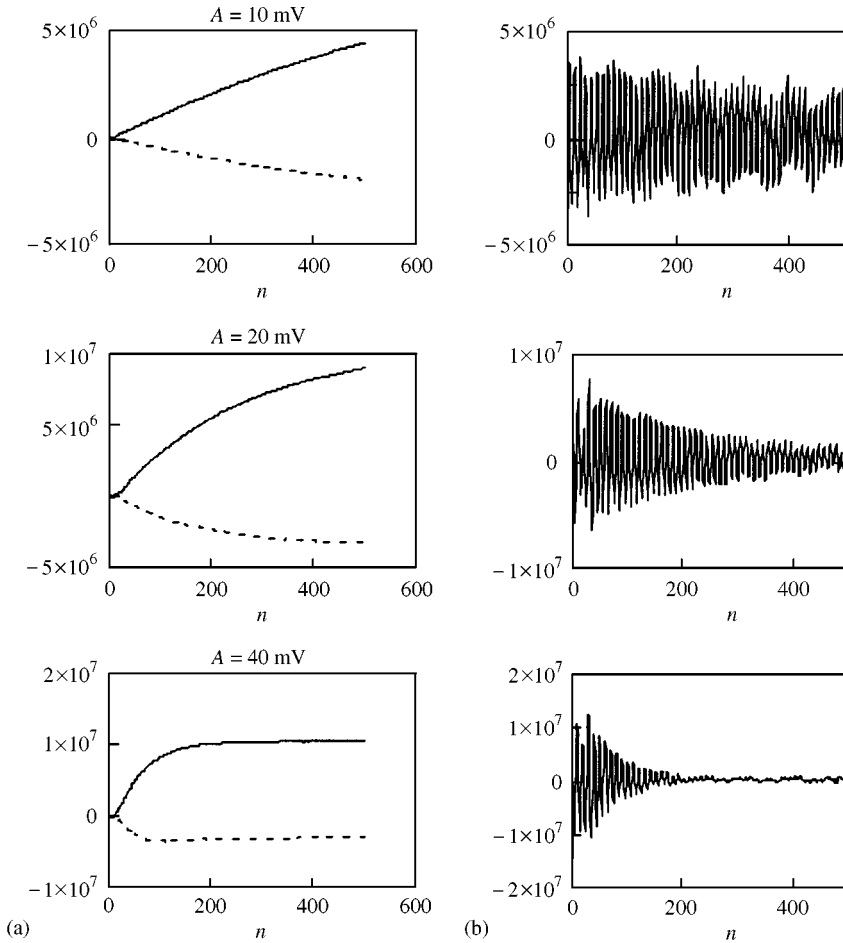
Figure 8. Adaptive speed at the centre of a stability band for three reference signal amplitudes $A = 10$, 20, and 40 mV. $PA = 5$, $\mu = 0.1$, $N - 2$, n_a 10, cancelling frequency $f_{ac} = 430$ Hz, $f_n = 4000$ Hz, $r_{sm} = 1$ m: (a) gives the FIR filter tap coefficient values and (b) shows the microphone error signal decay.

values typically diverge from zero setting to a symmetrical $\pm$ value, in the shape of a wish bone trajectory. This gives a good indication of the system operation. If the trajectories are not roughly symmetrical, then the system is not operating in the centre of its stability band.

3.4. SIDE BAND FREQUENCIES

Towards the edge of the stability band, the error signal shows modulation of the cancelling frequency in the time domain and side band frequencies on each side of the cancelling frequency in the frequency domain, as discussed in section 2.3. Now the satellite pole angle ϕ that determines the stability band position cannot be altered independently. It is a result of phase change of the system transfer functions, with frequency. Therefore it can only be altered, practically, by altering the cancelling frequency. Thus as β increases in value, the radius R of the phase circle increases and the circles distorts, the value of ϕ at the onset of instability, decreases, requiring that the cancelling frequency be reduced, which then decreases the phase angle ϕ to maintain stability. The net result as β increases is that
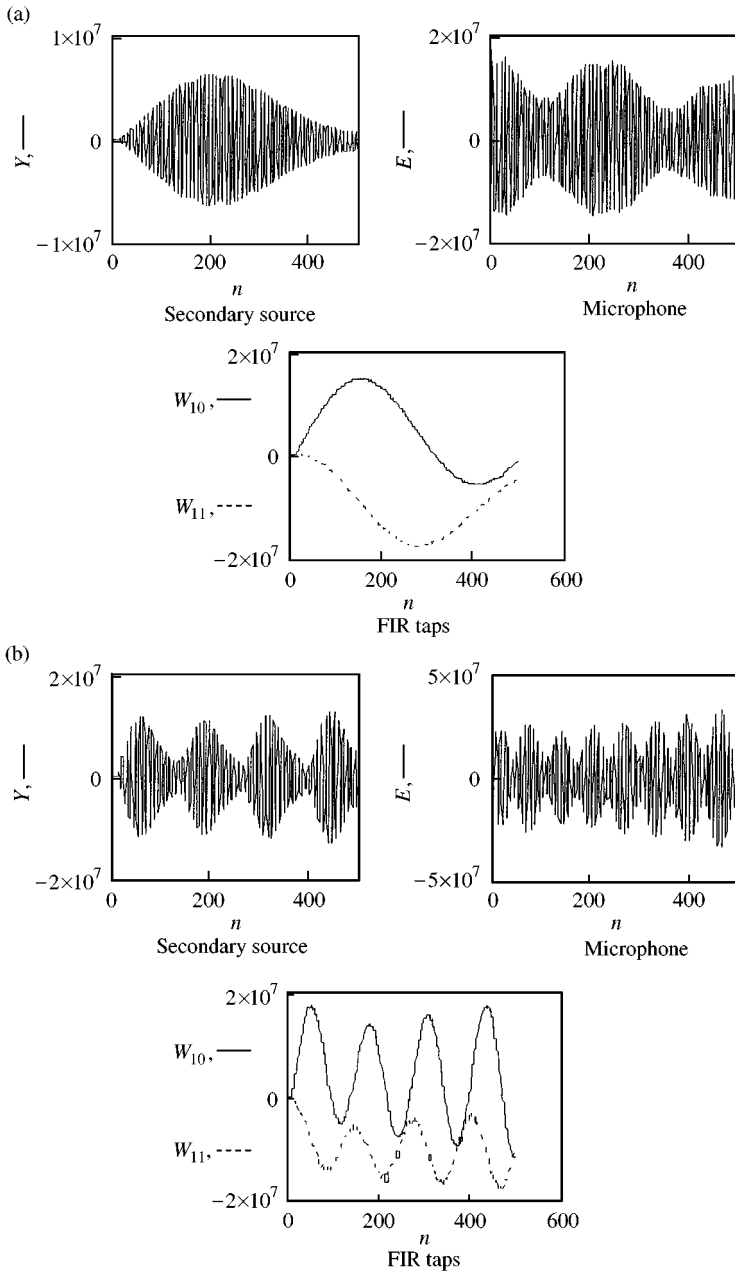
Figure 9. Modulated cancelling frequencies at the upper frequency edge of stability band for two reference signal amplitudes $A = 40$ and 80 mV, $PA = 5$, $\mu = 0.1$, $N-2$, n_a 10, $f_n = 4000$ Hz, $r_{sm} = 1$ m. (a) $A = 40$ mV, $\beta = 0.16 \times 10^{-3}$, $(f_{ac})_{upper} = 492$ Hz, $f_{mod} = 20$ Hz. (b) $A = 80$ mV, $\beta = 0.64 \times 10^{-3}$, $(f_{ac})_{upper} = 457$ Hz, $f_{mod} = 60$ Hz.

the stability bandwidth reduces, the cancelling frequency is decreased and the effective cancelling modulation frequency increases.

Figure 9 shows modulation of the time histories for the $N-2$ $n_a 10$ stability band. The measurements give the secondary source cancelling signal Y, the error signal at the microphone E and the two-tap (coefficient) trajectories of the FIR filter W. The data are

given for the upper frequency edge of the stability band, as can be seen in Figure 6(b), top curve. The reference signal amplitude is $A = 40$ mV ($\beta = 0.16 \times 10^{-3}$) in Figure 9(a) and $A = 80$ mV ($\beta = 0.64 \times 10^{-3}$) in Figure 9(b). The cancelling frequency f_{ac} corresponding to the upper edge of the stability band, decreases with increasing reference signal amplitude A, in accordance with Figure 6(b), whereas the modulation frequency f_{mod}, increases as indicated by equation (5a). The corresponding frequencies f_{ac} and f_{mod} (parenthesis) measured are 492 (20) Hz and 475 (60) Hz, for the two reference voltages, $A = 40$ and 80 mV respectively.

The cancelling frequency is measured with a spectrum analyzer and the modulation frequency is measured from Figure 9 using $1/nTn$, where n is the number of samples and T_n is the sampling period. This gives an effective satellite pole phase circle radius at the edge of the stability band from equation (5a) of $R = \omega_{mod}/f_n \equiv 360°(f_{mod}/f_n) \approx 2$ and $6°$ for the two successive increases in A. Also measured with the spectrum analyzer are the side band frequencies on each side of the cancelling frequency given by equation (5c) $f_{sb} = f_{ac} \pm f_{mod}$. These are 512 Hz, 472 Hz and 535 Hz; 415 Hz for the two values respectively. At the edge of the stability bands, the modulation frequency does not decay, generating persistent side band frequencies. At low levels of A and away from the edges of the stability band, the modulation frequencies are not obvious, generating side band frequencies close to cancelling frequency that decay rapidly. Finally, there is a measured low-amplitude difference frequency, generated between the cancelling frequency and the Nyquist frequency ($f_n/2$). This frequency becomes low and its amplitude significant when the frequency approaches the Nyquist frequency.

3.5. ADAPTIVE SPEED

Figure 10 shows the adaptive time constant τ_a (time for the error at the microphone to decay to 63% of its initial value) plotted in samples against the adaptive step size μ. These are measured at the centre of the stability band, for two levels of reference amplitude $A = 10$ and 320 mV. Again $r_{sm} = 1$ m and $f_n = 4$ kHz. The primary source power amplifier PA was adjusted to keep the sound pressure fairly constant for the two levels of the reference
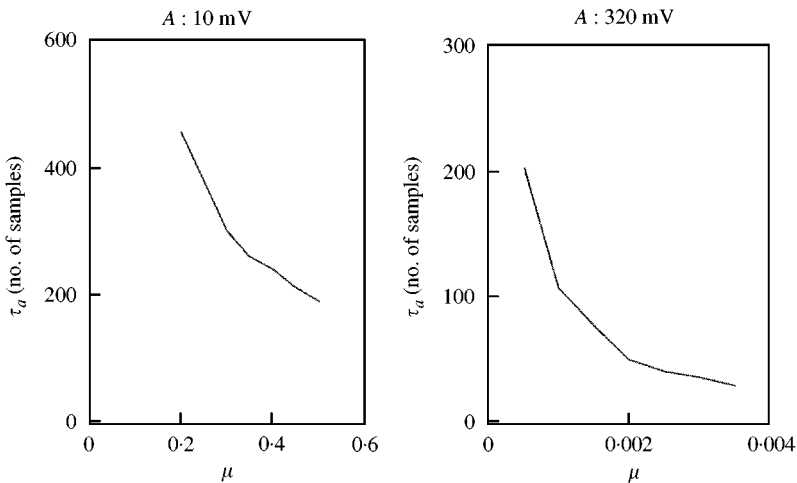

Figure 10. Adaptive time constant τ_a versus adaptive step size μ at the centre of stability band for reference inputs $A = 10$ and 320 mV. Stability region $N - 2$, $n_a = 10$, $r_{sm} = 1$ m. $r_{ps} = 0.3$ m, $f_{ac} = 385$ Hz, $f_n = 4000$ Hz.

amplitude A. It can be seen that the functions are rectangular hyperbolae of the form

$$\tau_a \beta = \kappa. \tag{10}$$

For values of τ_a in samples, the adaptive performance constant κ is approximately 10×10^{-3}, or in seconds ($\tau_a T_n$ where $T_n = 1/f_n$ and $f_n = 4000$), the value of the constant becomes $10\,000 \times 10^{-6}/f_n \approx 2\cdot5 \times 10^{-6}$. For a maximum value of $\beta \approx 0\cdot8 \times 10^{-3}$ for the $(N - 2\, n_a 10)$ stability band, in Figure 7, the smallest τ_a value is about 15 samples.

Figure 11(a) shows the decay rate for three propagation distances r_{sm} between the secondary source and the microphone of 1, 2 and 4 m, for a reference amplitude $A = 80$ mV. It can be seen that the adaptive performance constant is now given approximately by the inverse of the propagation distance, and thus equation (10) becomes

$$\tau_a \beta / r_{sm} = \kappa. \tag{11}$$

In addition, there are propagation distance delays τ_p, given by $n_r = (r_{sm}/c_0)f_n$, before any adaptive process can start. For the same three distances, these are 12, 24, and 48 samples, or 3, 6, and 12 ms. Thus the total convergence time is given by

$$\tau_t = \tau_a + \tau_p. \tag{12}$$

Substituting for τ_a and τ_p gives τ_t in samples as approximately

$$\tau_t \approx \tau_{sm}[(10^{-2}/\beta) + f_n/c_0]. \tag{13}$$

For example, if $A = 80$ mV and $\mu = 0\cdot1$ ($\beta = 640 \times 10^{-6}$) the first term in the brackets yields 16 samples and the second term 4000/340 yields 12 samples. Generally, τ_a is much larger than τ_p, except for very large β; also large r_{sm} makes both τ_a and τ_p large, so τ_a will usually dominate the response time.

Finally, Figure 11(b) shows the adaptive decay rates for three cancelling frequencies $f_{ac} = 200$, 400 and 800 Hz, at a source–microphone propagation distance $r_{sm} = 1$ m. It can be seen that κ approximately doubles for at least quadrupling in the cancelling frequency. Normalizing on $f_{ac} = 400$ Hz, equation (11) can now be represented by

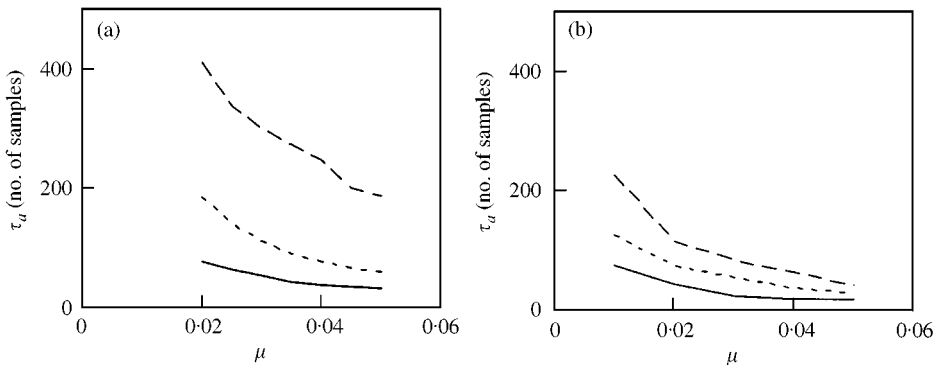$$\tau_a \mu A^2 (r_{sm})^g (f_{ac}/400)^h = \kappa, \tag{14}$$

Figure 11. Adaptive time constant τ_a versus adaptive step size, μ. (a) The curves for three propagation distances $r_{sm} = $ (——) 1, (– – – –) 2 and (——) 4 m for a cancelling frequency $f_{ac} = 400$ Hz. (b) The corresponding curves for three frequencies $f_{ac} = $ (——) 200, (– – – –) 400 and (——) 800 Hz at a propagation distance of $r_{sm} = 1$ m at $A = 80$ mV. Otherwise the same condition as Figure 10 holds.

where g and h are approximately -1 and $-\frac{1}{2}$ respectively. κ is the adaptive performance constant which depends on the particular laboratory set-up (system hardware and gains). The maximum adaptive speed is therefore achieved at short secondary source–microphone distances and low frequencies.

4. ACOUSTIC THEORY

After establishing the adaptive theory and measured adaptive performance of the basic canceller, the acoustic cancellation properties are now considered. The topics investigated are multipole sources to help understand the basic properties of acoustic sources, the acoustic characteristics of fundamental canceller and computed directivities at large distances and close to the source to compare with acoustic measurements made in the laboratory (section 5).

4.1. MULTIPOLE SOURCES

A series of complex classical sources called acoustic multipoles [15, 16] is briefly considered. In simple terms, the monopole is the basic acoustic source. Its radiation directivity is spherical or omni-directional (radiates equally in all directions) as radiated from a small loudspeaker housed in a closed box. This source is equivalent to introducing a time-varying fluid mass flow at a point in the propagating medium.

The next higher order source is the acoustic dipole. It comprises two monopoles, separated by a small distance apart, and driven out of phase by a fixed $180°$. The two sources tends to cancel each other's radiation, resulting in a figure-of-eight-shaped directivity. Maxima lie on the axis joining the two poles and minima at right angles to it. This source, which effectively exerts a force on the propagating fluid, is similar to that of an open loudspeaker, where each side of the diaphragm, relative to the propagating medium, is $\pm 90°$ out of phase.

The acoustic tripole is formed by placing a third monopole source in the centre of the dipole, on the line joining the poles. This third source has the same phase as one of the dipole sources, thus reinforcing the sound in the direction of that pole and cancelling the radiation in the direction of the other pole. Additionally, the added pole produces radiation on each side of the dipole axis, forming a cardioid or heart-shaped directivity.

Finally, a common (lateral) quadrupole is formed using four poles at the corner of a square, with diagonal poles of the same phase and adjacent poles of opposite phase. It can be considered as two parallel dipoles (forces) separated by a small distance, opposing each other (fluid stress). The resulting directivity is a four-leaf clover shape, with minima on the dipole axis and at right angles to it, forming four lobes (maxima) in between the minima at $45°$. These multiple sources constitute the four main radiation characteristics of classical acoustic sources found in nature.

4.2. FUNDAMENTAL CANCELLER

From an acoustics point of view, the single channel free-field canceller behaves as a special phase-controlled dipole. Here, the secondary source (canceller) combines with the primary source (source to be cancelled) to form a dipole. A detection system (microphone) is placed on the secondary source side and positioned along the so-formed dipole axis (line joining the two sources) to monitor the combined sound from both sources. The situation is

illustrated in Figure 1. Unlike the fixed phase of the classical multipoles, the phase and amplitude of the secondary source is adjusted automatically to minimize the sound at the detector.

The closer the primary and secondary sources are to each other (small r_{ps}) and the further away the detector (large r_{sm}), the more intense the cancellation. This phase-controlled dipole can simulate dipole-, tripole- and quadrupole-like source directivities, depending on the source frequency and separation distance between the primary and secondary sources. The properties of these sources are considered in more detail in reference [4] in section 5.

The acoustic model in the following computations uses point sources. Here the propagating (radiation) terms are included, but the near-field geometric terms, which are appreciable at high frequencies, and reactive terms which are appreciable at low frequencies, are neglected. This is considered adequate for small but finite sources, as discussed further in reference [2] in section 3. The sound pressure contours (equal levels) are given in dB's relative to the threshold of hearing (2×10^{-5} Pa).

4.3. COMPUTED DIRECTIVITIES

In Figure 12, the sound pressure is computed for the fundamental canceller up to a propagation distance of ± 100 m. The dipole is positioned in a vertical direction. Two small (point) sources constituting the dipole are situated at three primary–secondary source distances $r_{ps} = 0.3$ m ($\approx \lambda/4$), 0.43 m ($\lambda/2$) and 0.86 m (λ), where λ is the acoustic wavelength. The primary source–microphone distance $r_{pm} = 10$ m and the primary source strength and frequency are 1 m^3/s and $f = 400$ Hz respectively. The cardioid, figure-of-eight- and the four-leaf-clover-shaped directivities corresponding to the tripole-, dipole- and quadrupole-like directivities are clearly seen. Unlike the classical dipole, the figure-of-eight directivity for the phase controlled dipole is now oriented at 90° to the dipole axis.

The cardioid has the deepest cancellation (shadow depth) situated on axis at 0°, followed by the figure-of-eight and then the four-leaf clover. Shadows are usually defined as $20 \log_{10}$ of the ratio of primary source sound alone divided by the primary and secondary source sound together, measured at the same observation point. The shadows here, for convenience of display (only have to use one figure), are defined as $20 \log_{10}$ maximum sound divided by minimum sound at the same primary source–observer distance r_{po}, minus 6 dB for doubling of sound pressure at the maximum contributed by both sources. These are successively, for the cardioid, figure-of-eight and the four-leaf clover at $r_{po} = 80$ m, approximately $108 - 75 - 6 = 27$, $180 - 78 - 6 = 24$ and $108 - 83 - 6 = 19$ dB. These shadows have roughly equal cancellation on one (0°), two (0, 180°) and all four (0, 90, 180, 360°) sides respectively.

Figure 13 computes the cardioid directivity ($r_{ps} = 0.3$ m) for $f = 400$ Hz and three primary–microphone distances $r_{pm} = 1$, 10 and 100 m. It shows that the shadow becomes narrower and deeper as r_{pm} increases. At a distance $r_{po} = 80$ m, the cancellation is approximately $107 - 93 - 6 = 8$, $108 - 75 - 6 = 27$ and $110 - 40 - 6 = 64$ dB respectively for the three increasing distances. These computations indicate that deep shadows, propagating into the far field, are theoretically possible using this basic canceller.

4.4. DIRECTIVITIES CLOSE TO SOURCE

The following figures give the corresponding sound pressure contours computed close to the source, for comparison with measurements that can be made in the laboratory.
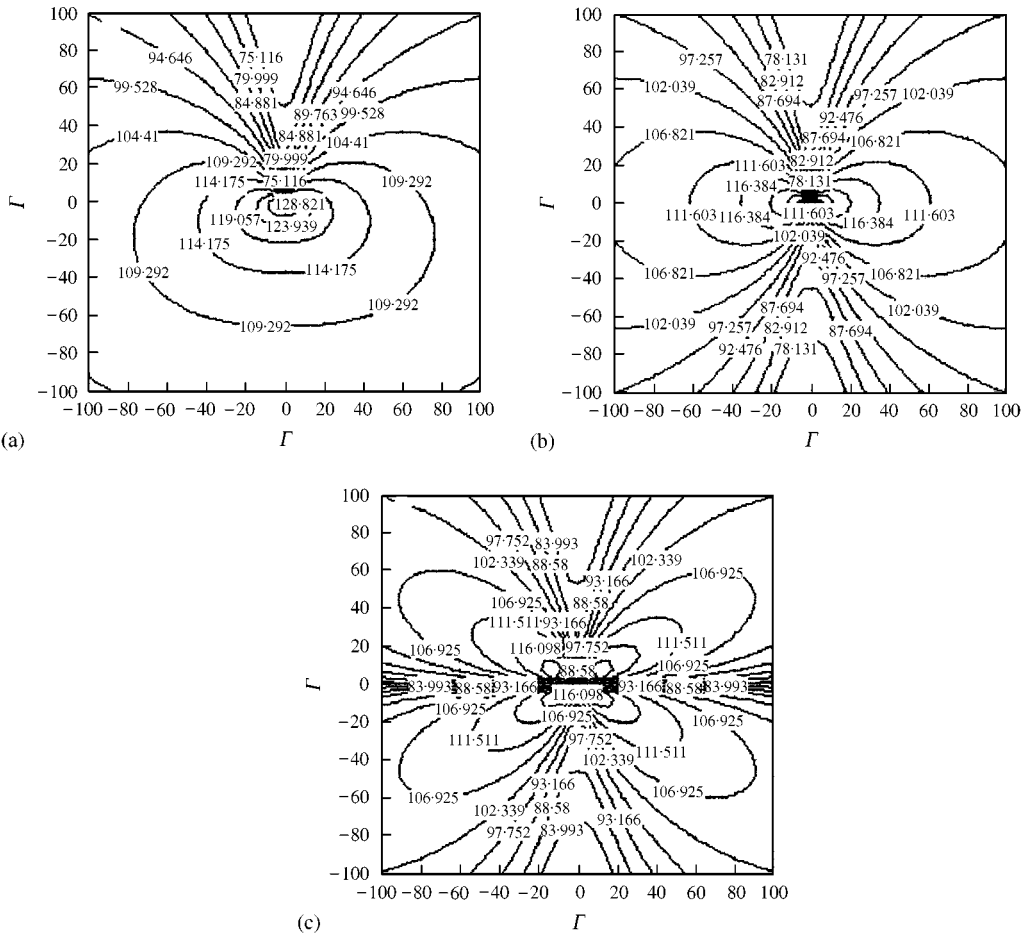
Figure 12. Sound pressure contours (dB versus distance in m) of basic canceller (far field) for 3 primary–secondary source distances $r_{ps} = 0.3$, 0.429 and 0.8575 m, $p = 1$, $s = 1$, $f_{ac} = 400$ Hz, $r_{pm} = 10$ m. (a) $r_{ps} = 0.3$ m ($< \lambda/2$) "tripole like", (b) $r_{ps} = 0.429$ m ($\lambda/2$) "dipole like", (c) $r_{ps} = 0.8575$ m (λ) "quadrupole like".

Figure 14 shows the tripole-, dipole- and quadrupole-like directivities over a ± 2 m distance around the source for a primary source–microphone distance $r_{pm} = 1$ m. The series of tightly packed circles around the origin is due to the steeply rising sound field very close to the primary and secondary sources. The corresponding cardioid, figure-of-eight and the four-leaf clover patterns are just about recognizable (compare with Figure 12 for the distant field). The cancellation depth, at a primary source–observer distance $r_{po} = 2$ m front and rear, front and side and front and $45°$ are approximately $140 - 123 - 6 = 11$, $140 - 127 - 6 = 7$ and $140 - 134 - 6 = 0$ dB respectively.

Figure 15 shows the sound pressure contours computed over ± 10 m, for 400 Hz, the cardioid source ($r_{ps} = 0.3$ m) and for three primary source–microphone distances $r_{pm} = 1$, 2 and 4 m. The shadows increase and become narrower with increasing r_{pm}. At a primary source–observer distance $r_{po} = 4$ m the shadow levels are approximately $131 - 116 - 6 = 9$, $132 - 106 - 6 = 20$ and $132 - 92 - 6 = 34$ dB, respectively, increasing at more than 6 dB per doubling in distance. The level at $r_{po} \approx 4$ m is very small, at $r_{pm} = 4$ m the level is, of course, theoretically zero (a singularity). Therefore, the level with the observer microphone down stream and close to the detector microphone, where the shadow level is fairly constant, is used.
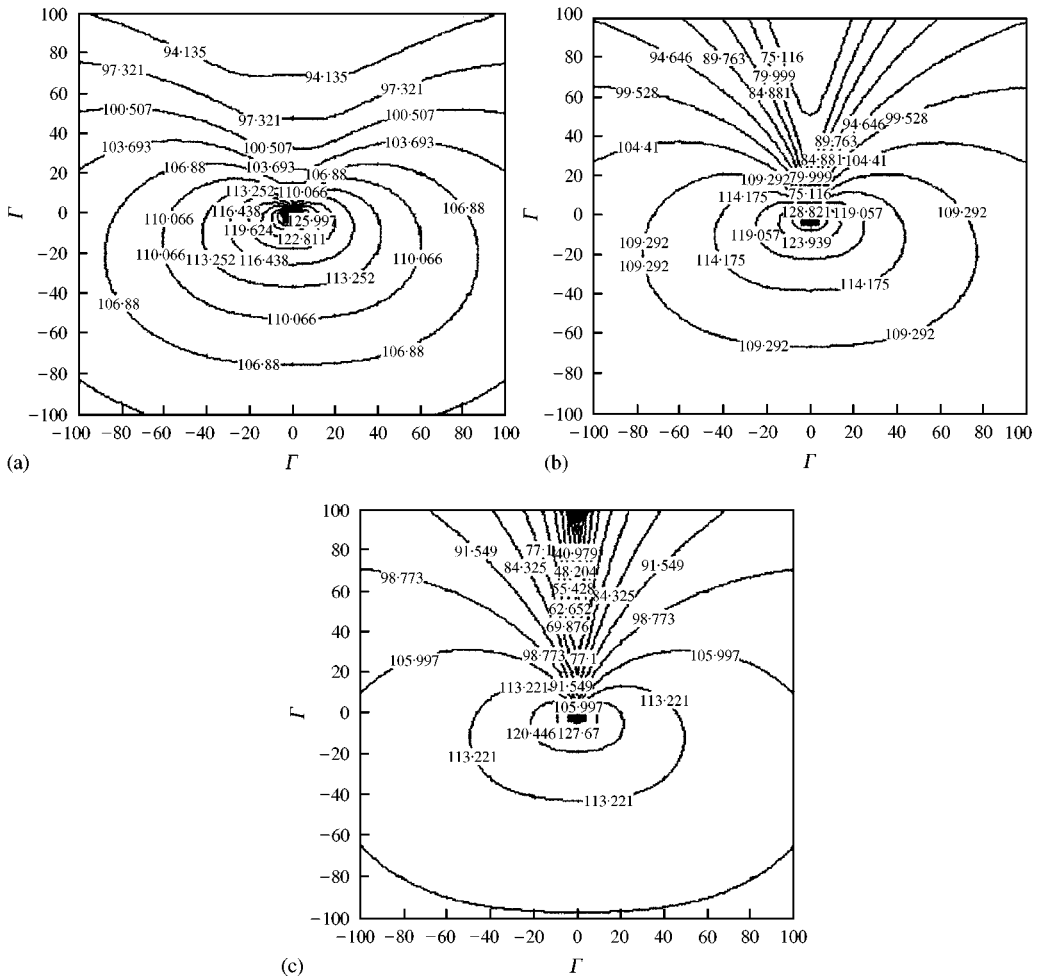
Figure 13. Sound pressure contours (dB versus distance in m) of tripole-like basic canceller (far field) for three primary source–microphone distances $r_{pm} = 1$ (a), 10 (b) and 100 m (c), $f_{ac} = 400$ Hz, $p = 1$, $s = 1$, $r_{ps} = 0.3$ m.

Finally, Figure 16 shows the sound pressure contours over ± 2 m for the cardioid source for $r_{pm} = 1$ m, and three source frequencies 200, 400 and 800 Hz. The cancellation depth for all three frequencies is approximately 14 dB (i.e., $135 - 115 - 6$, $141 - 121 - 6$, and $147 - 127 - 6$ respectively). However, the shadow becomes narrower with increasing frequency. Note that the sound pressure directivity at 800 Hz is beginning to resemble the four-leaf clover directivity as the wavelength $\lambda = c_0/f = 0.43$ m approaches the primary–secondary source separation distance $r_{ps} = 0.3$ m, giving a maximum at about 75° and a minimum at about 105° (behind the source). Also, the sound increases generally at about 6 dB per octave, per doubling in frequency, for the same (constant) primary source strength of 1 m^3/s.

5. ACOUSTIC MEASUREMENTS

After establishing the acoustic characteristics of the basic canceller, the measured acoustic performance of the canceller is now considered. The computer predictions discussed in
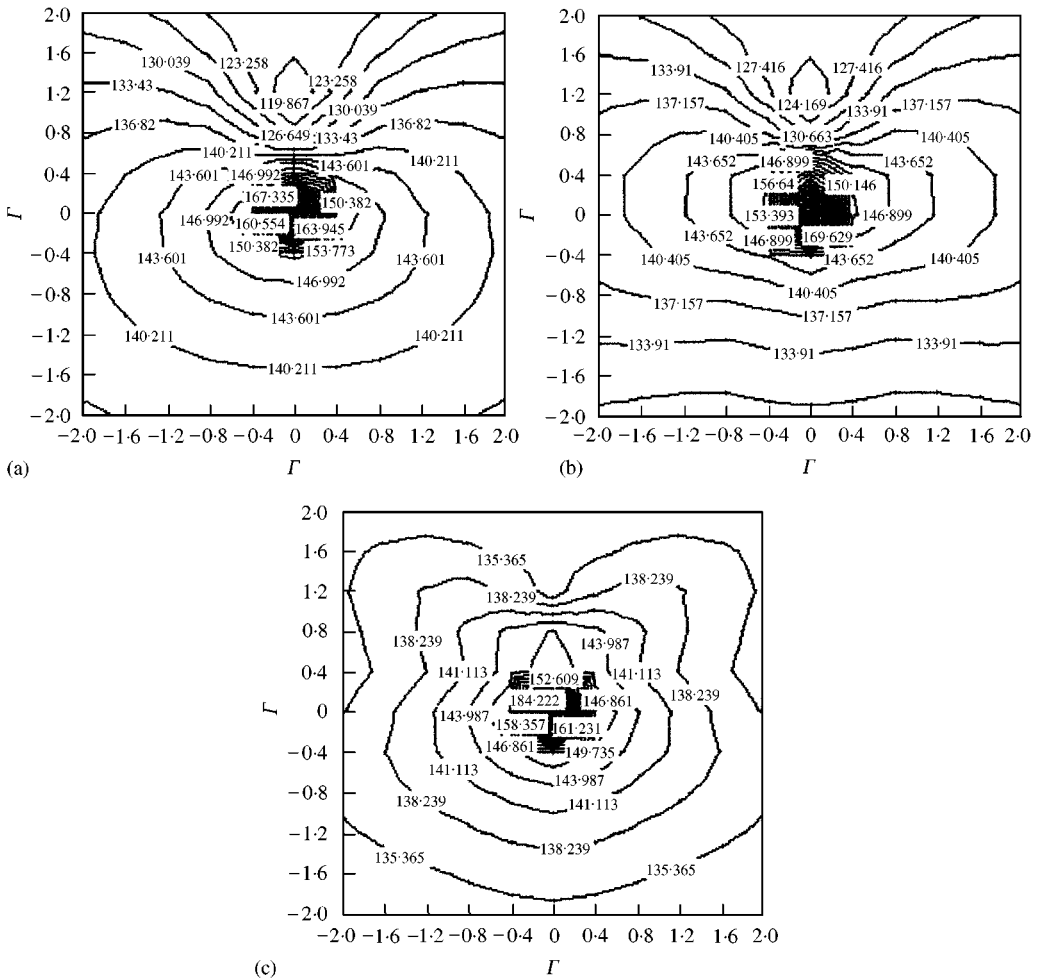
Figure 14. Sound pressure contours (dB versus distance in m) of basic canceller (near field) for three primary–secondary source distances $r_{ps} = 0.3$ m ($\approx \lambda/4$, "tripole-like"), (a) 0.429 m ($\lambda/2$, "dipole-like"), (b) and 0.8575 m (λ, "quadrupole-like"), (c) $p = 1$, $s = 1$, $f_{ac} = 400$ Hz, $r_{pm} = 1$ m.

section 4 are for hypothetical point acoustic sources, which do not exist in practice. The measurements below are an attempt to verify these theoretical predictions using real (finite) acoustic sources and detectors. The very presence of these transducers will necessarily modify the resultant acoustic field. The sound radiation characteristics produced by the fundamental cancelling source, after full convergence of the adaptive process, are now considered.

5.1. MEASUREMENT DETAILS

The following figures show the actual sound pressure directivities (equal measurement distances around the source) measured on a 5 m × 5 m floor area and 4 m high anechoic facility at the University of Huddersfield. The surfaces were treated with 10 cm thick surface coated dense fibre glass (4.3 kg m/m³), which is nominally 100% absorbing for frequencies
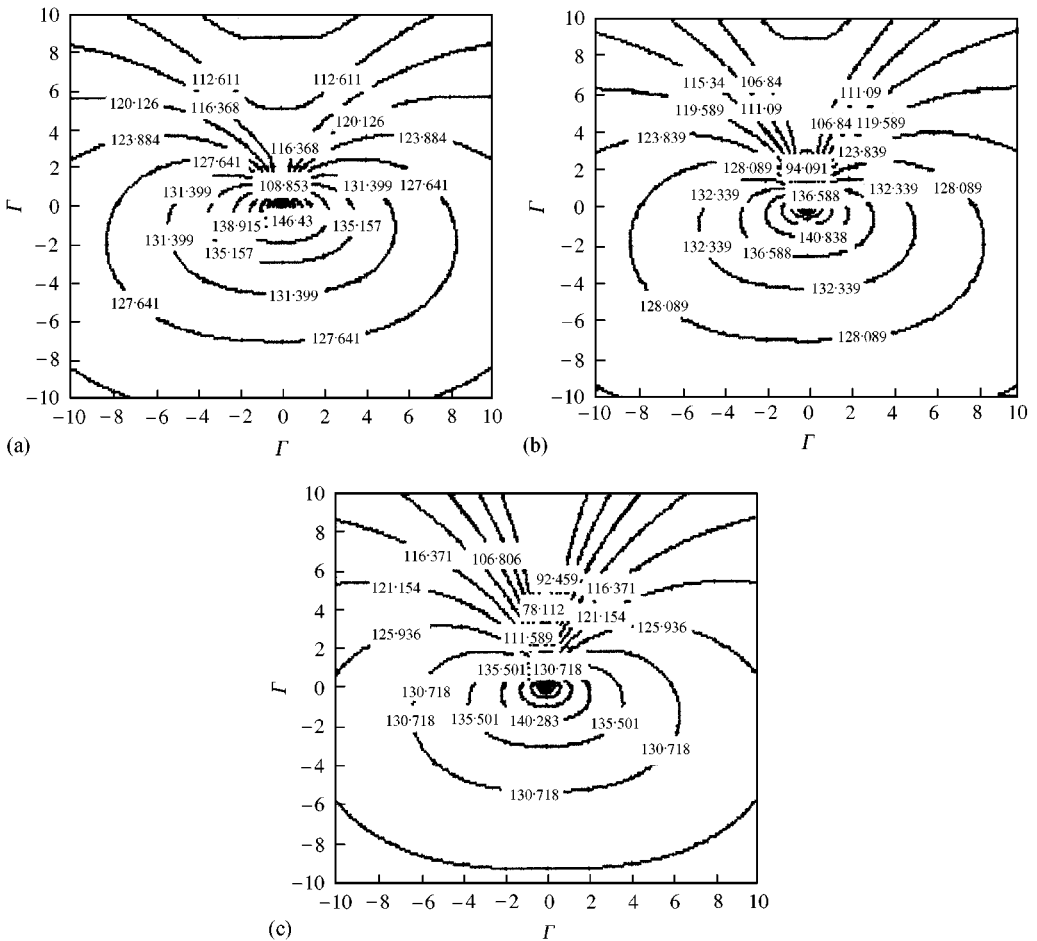
Figure 15. Sound pressure contours (dB versus distance in m) of basic 'tripole' canceller (near field) for three primary source–microphone distances $r_{pm} = 1$ (a), 2 (b) and 4 m (c), $f_{ac} = 400$ Hz, $p = 1$, $s = 1$, $r_{ps} = 0.3$.

above 200 Hz. The primary and secondary sources comprise a 10 cm loudspeaker housed in a 0.2 m enclosure, giving basically an omni-directional radiation directivity over the frequency range of interest (200–800 Hz), with slightly higher sound (≈ 3 dB) in front of the speaker. The system set-up is illustrated in Figure 1.

The microphones used were of an inexpensive piezoelectric type, whose frequency responses were measured and their gains corrected at the computer input. The array of microphones, used to measure the sound directivities, were automatically sampled successively and plotted using an in-house developed program. The $N - 2$, n_a10 stability region at 400 Hz, (see Figure 6), with reference to signal amplitude $A = 40$ mV, adaptive step size $\mu = 0.1$ ($\beta = 0.16 \times 10^{-3}$), primary source power amplifier $PA = 5$, $r_{ps} = 0.3$ m (minimum distance limited by the support speaker stands), $r_{pm} = 1$ m and $r_{po} = 2$ m were used generally.

The cancellation levels depend on the reference amplitude A, primary power amplifier setting PA, stability region used and where within the region the system is operated, (ideally in the centre of the region, giving > 60 dB at the detection microphone), as explained in section 3.2. Variability in the cancellation depth, particularly at the higher frequencies
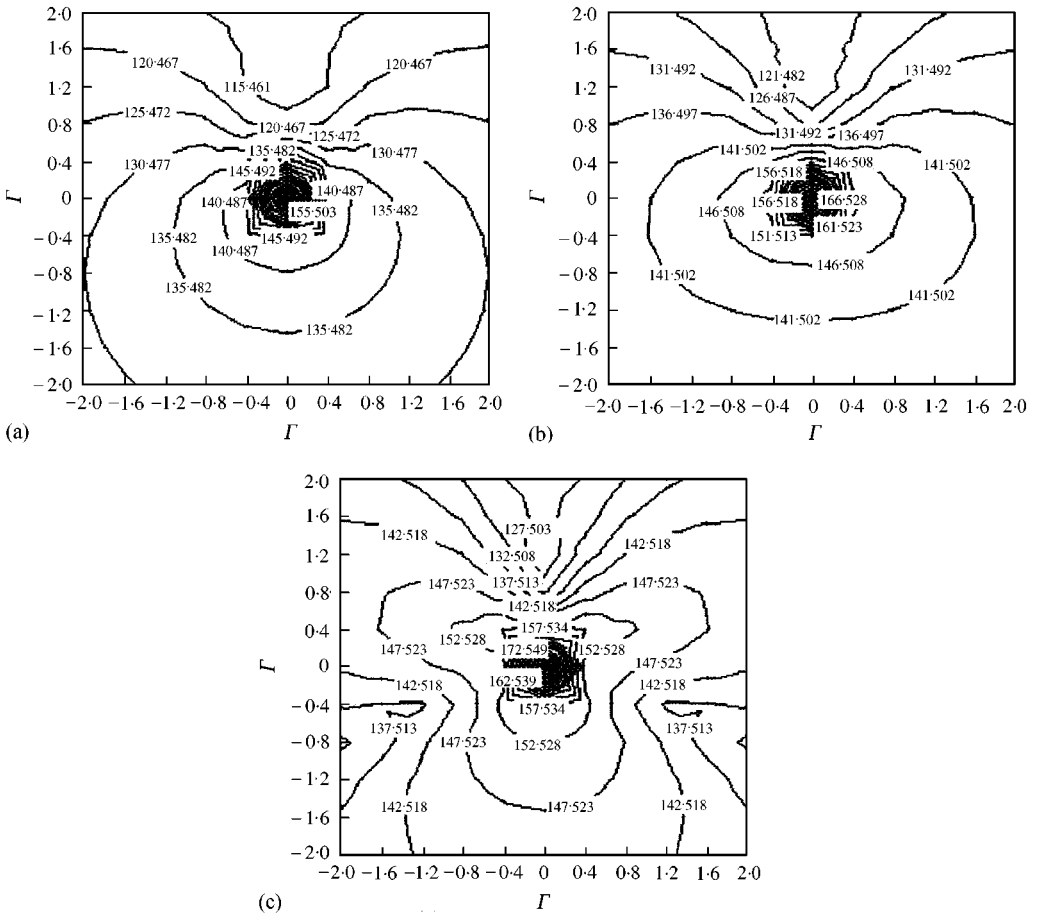
Figure 16. Sound pressure contours (dB versus distance in m) of basic "tripole' canceller (near field) for three radiation frequencies $f_{ac} = 200$ (a), 400 (b) and 800 (c) Hz, $p = 1$, $s = 1$, $r_{ps} = 0.3$ m, $r_{pm} = 1$ m.

(400 and 800 Hz) depends on the alignment between the primary source, secondary source and the detector, as well as on reflections between the primary and secondary sources, which in turn depend on the degree of cover up of the primary source by the secondary source. This interference is minimized by non-line-of-sight alignment of the sources.

The presence of the secondary source also affects the uncancelled sound directivity. Complete alignment (100% coverage of the primary source by the secondary source) reduces the sound along the axis at 0°, complete uncovering increases the sound along the axis and 50% coverage produces a fairly omni-directional directivity. Due to the room size, most of the measurements were taken over 180°, and mirrored for the other 180°, the 4 m observer distance was measured over a quadrant only (90°). The primary–secondary source dipole axis in the directivities is now oriented horizontally.

5.2. ACOUSTIC PERFORMANCE

Figure 17 shows the measured tripole-, dipole- and quadrupole-like directivities (measurements made at a fixed distance from the primary sources and over an observer
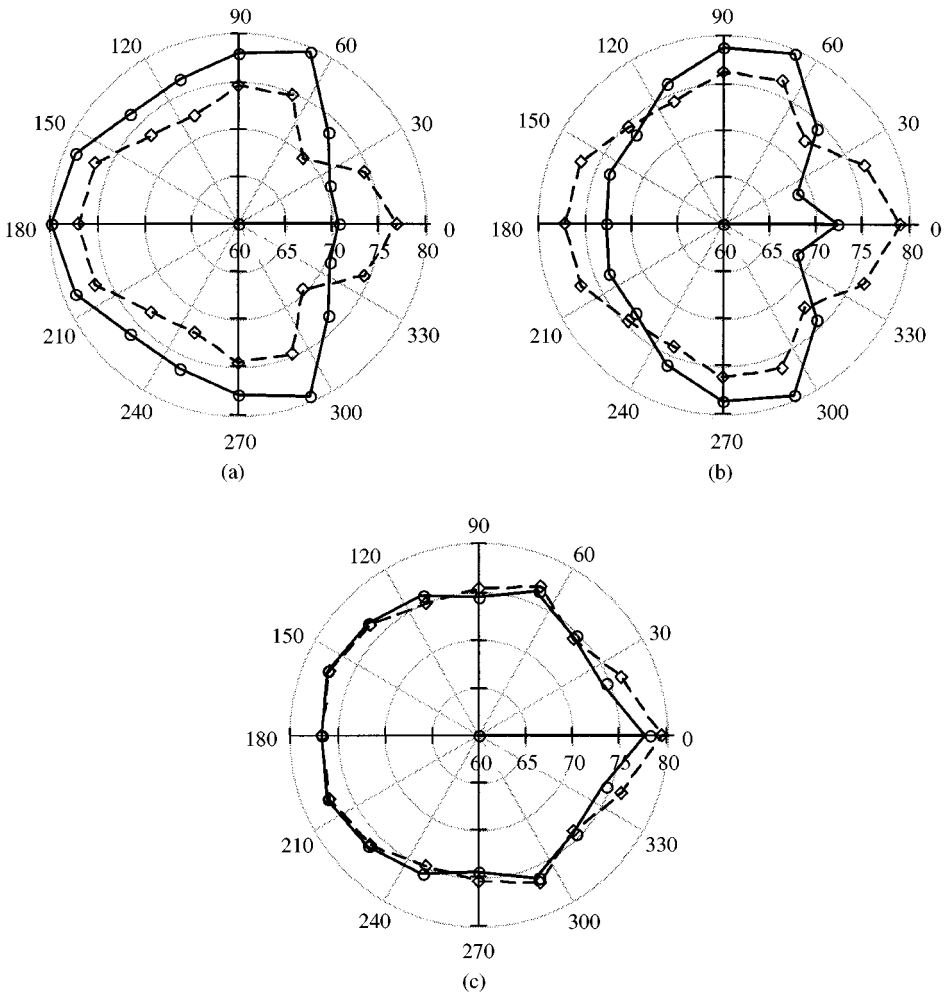
Figure 17. Measured sound pressure directivities (dB versus observer angle φ) for three primary–secondary source distances $r_{ps} = 0.30$ (a), 0.43 (b) and 0.86 m (c), frequency $f_{ac} = 400$ Hz, $r_{pm} = 1$ m, $r_{po} = 2$ m: $\diamond$, uncancelled system; $\ominus$, cancelled system.

angle $\varphi = 0 \to 360°$). The primary–secondary source separation distances are $r_{ps} = 0.3$ m ($\approx \lambda/4$), 0.43 m ($\lambda/2$) and 0.86 m (λ). The primary source–microphone distance is $r_{pm} = 1$ m, the primary source–observer distance (measurement radius) is $r_{po} = 2$ m and the acoustic source frequency is $f_{ac} = 400$ Hz. The measured directivities have similar characteristics to those computed in Figure 14. There is reduced radiation at 0° in the case of the tripole, reduced radiation at 0 and 180° in the dipole-type case and slightly reduced radiation at 0 and $\pm 90°$ in the quadrupole-type case with no increases in radiation at any other angle. The quadrupole directivity measured at $r_{pm} = 2$ m (not shown) provided appreciable sound reductions at 0, ± 90 and 180°.

The cancellation depths at 0° (difference between cancellation on and off at the same measurement point, $r_{po} = 2$ m) are about 6, 7 and 1 dB for the tripole-, dipole- and quadrupole-type sources respectively. These compare roughly with 11, 7 and 0 dB in Figure 14 for the computed values. These measurements support the predictions that these sources would in fact produce well-defined cardioid, figure-of-eight and the four-leaf clover patterns in the far field, as computed in Figure 12.
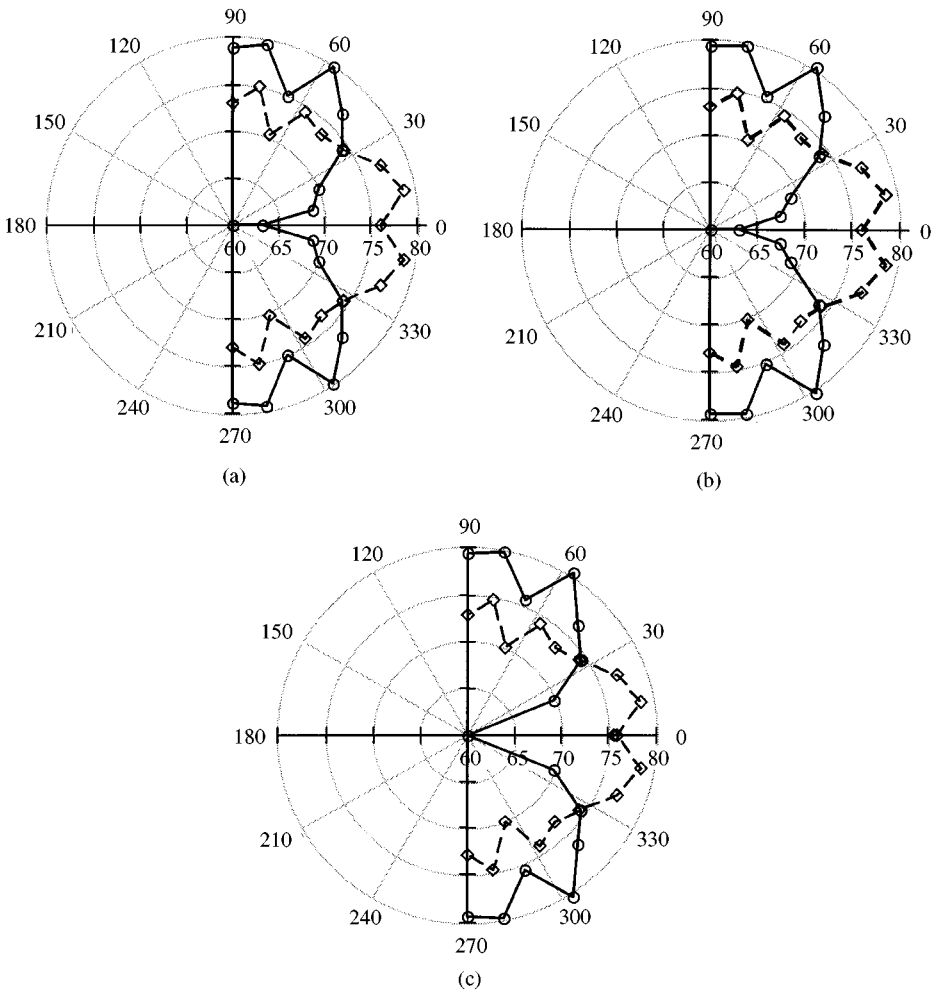
(a)

(b)

(c)

Figure 18. Measured sound pressure directivities (dB versus observer angle φ) for three primary source–microphone distances $r_{pm} = 1$ (a), 2 (b) and 4 m (c), frequency $f_{ac} = 400$ Hz, $r_{po} = 4$ m, $r_{ps} = 0.3$ m: $-\diamondsuit-$, uncancelled system; $-\ominus-$, cancelled system.

Figure 18 shows the sound pressure for three primary source–microphone distances $r_{pm} = 1, 2, 4$ m, and primary source–observer distance of $r_{po} = 4$ m. The primary–secondary source distance $r_{ps} = 0.3$ m and the source frequency was 400 Hz. The $N - 1$ stability region was used for $n_a = 11, 14$ and 15, for the three r_{pm} distances respectively. The measurements were made over 90° only, because of the limited room size. Generally, the cardioid shadow depth deepens and narrows as r_{pm} increases. The values at $\varphi = 0°$ are 12, 12 and 18 dB for the three distances $r_{pm} = 1, 2$ and 4 m respectively. These compare with corresponding values of 9, 20 and 34 dB in Figure 15 for the theoretical values.

Figure 19 shows the sound pressure directivity for the cardioid source for three source frequencies $f = 200$ Hz (stability region $n_a 14$ $N - 1$), 400 Hz ($n_a 10$ $N - 2$) and 800 Hz ($n_a 20$ $N - 3$) (see section 3.2 and Figure 6 for further details on stability regions). The primary–secondary source distance $r_{ps} = 0.3$ m, the primary source–microphone distance $r_{pm} = 1$ m and the primary source–observer distance $r_{po} = 2$ m. The measured cancellation depths centered at $\varphi = 0°$ were approximately 10, 7, 14 dB for the three frequencies respectively, the shadow becoming narrower as the frequency increases. These results
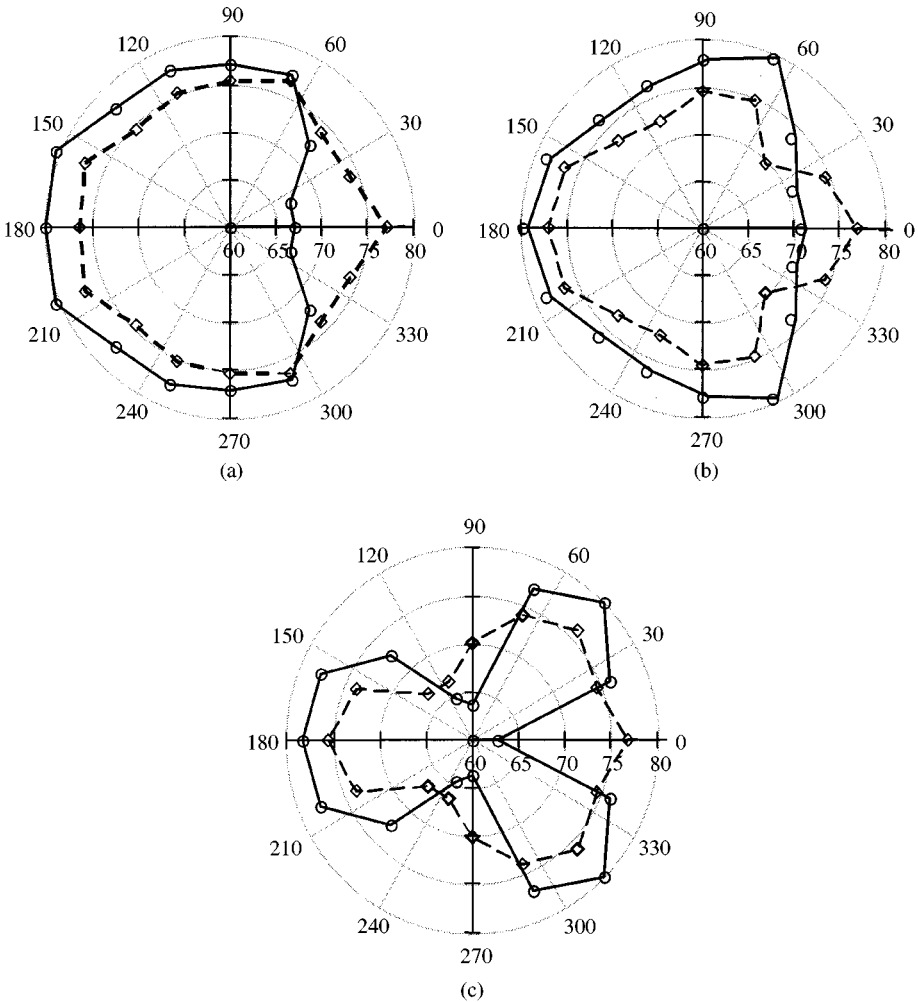
Figure 19. Measured sound pressure directivities (dB versus observer angle φ) for three source frequencies (a) $f_{ac} = 200$, (b) 400 and (c) 800 Hz, $r_{pm} = 1$ m, $r_{po} = 2$ m, $r_{ps} = 0.3$ m: —◇—, uncancelled system; —⊖—, cancelled system.

compare well with Figure 16 for the computed results of about 14 dB for all three frequencies. Generally, the measurements show a maximum greater than $\varphi = 90°$ for the lower frequencies and a minimum greater than $\varphi = 90°$ at 800 Hz, similar to the theoretical results given in Figure 16.

Finally, Figure 20 gives the shadow depth as a function of primary source–observer distance r_{po} along the sources–microphone alignment axis ($\varphi = 0$), for $r_{ps} = 0.3$ m, $r_{pm} = 2$ m and three acoustic source frequencies $f_{ac} = 200$, 400 and 800 Hz. The maximum shadow depth occurs for the observer microphone close to the detector microphone (the closest that it can physically be is a microphone diameter from $r_{pm} = 2$ m), the levels at the actual detector being > 60 dB (dynamic range of the system). The shadows increase fairly uniformly from the source to the detector. Beyond the detector the shadow levels approach about 15 dB for the three frequencies, the levels depending critically on the primary, secondary and microphone alignment. This compares with the theoretical value of about 20 dB, as predicted in Figure 15. Level variations also occur, which are reduced by minimizing reflections particularly between the primary and secondary source.
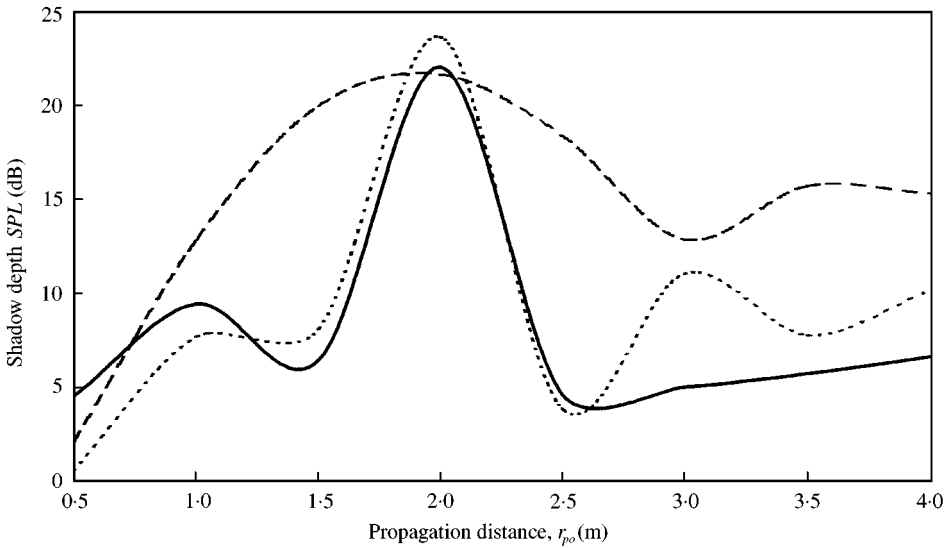
Figure 20. Measured shadow depth versus propagation distance r_{po} for three frequencies f_{ac} = (– – – –) 200, (———) 400 and (- - - - -) 800 Hz, r_{pm} = 2 m, r_{ps} = 0·3 m, A = 40 mV, PA = 5, $N-3$, n_a 19 (f_{ac} = 200 Hz), $N-3$, n_a 25 (f_{ac} = 400 Hz), $N-3$, n_a 16 (f_{ac} = 800 Hz).

In summary it can be said that reasonable agreement has been achieved between the acoustic theory and the laboratory measurements, despite the practical problems involved.

6. CONCLUSIONS

The basic adaptive process and the measured performance of a single channel free-field sound cancelling system have been investigated. It has been shown that the system has poles situated on concentric phase circles surrounding the zeros lying on the z-plane unit circle. These satellite poles rotate according to the phase difference between the primary field and the cancelling field, generated by the system transfer function. These rotations produce a series of stability bands that have complex behaviour, as the cancelling strength β increases, resulting in band contraction and band splitting.

Satellite pole frequencies corresponding to the edge of the stability bands modulate the cancelling frequency to generate unwanted sum and difference side band frequencies, in addition to the cancelling frequency. The characteristics of the stability process are established in detail, including the stability band positions, widths, and side band frequency generation. Unlike the in-phase systems whose maximum β value for assured stability operation is 2, these systems can remain stable for much larger values of β up to 12.

The stability band width decreases and adaptive speed increases as the cancelling strength β increases; i.e., the product of adaptive step size and reference input squared ($\beta = \mu A^2$). The onset of zero bandwidth is typically around $\beta = 0·8 \times 10^{-3}$ where A is in mV. The adaptive performance constant κ for the particular laboratory set-up can be represented by $\kappa = \tau_a \beta (r_{sm})^g (f_{ac}/400)^h \approx 10 \times 10^{-3}$, where g and h are approximately -1 and $-\frac{1}{2}$ respectively. τ_a is the adaptive time constant in samples, r_{sm} is the secondary source–microphone distance in m and f_{ac} is the acoustic cancelling frequency in Hz. Decreasing κ increases the adaptive speed.

Although this mechanism has an almost infinite number of unstable as well as stable bands, the system is basically stable. Without intentional correlated cancellation excitation,

the unstable bands have zero phase circle radius ($\beta = 0$). Thus the poles cannot lie outside the unit circle, making the system at worst marginally stable. Although the stability regions, have different eigenvalues and are therefore unique, their basic characteristics are similar.

The radiation characteristics and sound cancellation performance of the fundamental canceller, both theoretical and hardware implemented, have been established. The basic radiation directivity pattern depends on the primary–secondary source separation distance r_{ps}. It is similar to a tripole, dipole or quadrupole source for $r_{ps} = \lambda/4, \lambda/2$ and λ, respectively, where λ is the acoustic wavelength. The cancellation depth increases with decreases in r_{ps}, increases with increases in secondary source–microphone distance r_{sm} and source–observer distance r_{po} and becomes sharper (narrower) with increases in frequency.

The laboratory measurements of the basic single-channel system compare well with the theoretical predictions given by computer modelling. This gives confidence in predicting the radiation properties at large distances from the source and supports the notion that deep shadows generated by multichannel systems, implemented into hardware, can also be realizable.

ACKNOWLEDGMENT

REFERENCES

1. S. E. WRIGHT and B. VUKSANOVIC 1996. *Journal of Sound and Vibration* **190**, 565–585. Active control of environmental noise, I.
2. S. E. WRIGHT and B. VUKSANOVIC 1997 *Journal of Sound and Vibration* **202**, 313–359. Active control of environmental noise, II: non-compact acoustic sources.
3. S. E. WRIGHT and B. VUKSANOVIC 1999 *Journal of Sound and Vibration* **220**, 469–496. Active control of environmental noise, III: implementation of theory into practice.
4. S. E. WRIGHT and B. VUKSANOVIC 1999 *Journal of Sound and Vibration* **222**, 635–668. Active control of environmental noise, IV: practical extensions to ECAS theory.
5. S. E. WRIGHT and H. ATMOKO 2001 *Journal of Sound and Vibration* **244**, 107–122. Active control of environmental noise, V: effect of environmental change on the stability of free-field sound cancelling systems.
6. S. J. ELLIOTT, I. M. STOTHERS and P. A. NELSON 1987 *IEEE Transactions on Acoustics, Speech, and Signal Processing* **35**, 1423–1434. A multiple error LMS algorithm and it's application to the active control of sound and vibration.
7. S. KUO and D. MORGAN 1996 *Active Noise Control* New York: John Wiley and Sons.
8. P. A. NELSON and S. J. ELLIOTT 1992 *Active Control of Sound* New York: Academic Press.
9. J. F. ABBOT 1993 *International Conference on Acoustical Speech and Signal Processing* Vol V, 630–633. Acoustic design criteria for active noise control systems.
10. B. WIDROW, D. SHUR and S. SHAFFER 1981 *Proceedings of the 15th Asilomar Conference* 185–189. On adaptive inverse control.
11. J. C. BURGESS 1981 *Journal of Acoustical Society of America* **70**, 715–726. Active adaptive sound control in a duct: a computer simulation.
12. E. ZIEGLER 1989 U.S. Patent 4878188. Selective active cancellation system for repetitive phenomena.
13. B. WIDROW, J. R. GLOVER, J. M. MCCOOL, J. KAUNITZ, C. S. WILLIAMS, R. H. HERN, J. R. ZIEGLER, E. DONG and R. C. GOODLIN 1975 *Proceedings of the IEEE*, **63**, 1692–1716. Adaptive noise cancelling, principles and applications.
14. S. J. ELLIOT and P. A. NELSON 1985 *ISVR Technical Report No.* 136. The application of adaptive filtering to the active control of sound and vibration.
15. P. E. DOAK 1965 *Proceeding of the Fifth International Congress on Acoustics, Liege*, Paper K56. Multipole analysis of acoustic radiation.
16. S. E. WRIGHT 1986 *Journal of Sound and Vibration* **108**, 361–378. Sources and observers in motion I: time variant analysis and its implications for aerodynamic sound.